# High-Statistics Photonuclear Measurements of Short-Range Correlations

A. Somov, H. Szumila-Vance
Thomas Jefferson National Accelerator Facility,
Newport News, Virginia 23606, USA

O. Hen, J. R. Pybus
Massachusetts Institute of Technology, Cambridge, Massachusetts 02139, USA

T. Kolar
Tel-Aviv University, Tel Aviv 69978, Israel

A. Schmidt
The George Washington University, Washington, D.C. 20052, USA

**Abstract**

Short-ranged correlated (SRC) pairs of nucleons compose about 20% of nucleons in medium to heavy nuclei, and have a substantial impact on the structure of the nucleus. Recent years have seen significant progress in our ability to study SRC pairs using semi-inclusive and exclusive measurements of hard SRC breakup. Interpreting these measurements requires detailed understanding of the reaction mechanisms.

Recent photonuclear data using the Hall D photon beam have enabled the first measurements of SRC pair breakup using hard quasi-elastic meson photoproduction channels. These measurements have established the possibility of measuring SRC pairs using real photoproduction in the GlueX detector, and enable measurement of $A$-dependent properties. However, the quantity of data remains a relatively small sample, enabling establishment of basic SRC properties but not allowing precision measurements.

A high-statistics measurement using hard photonuclear reactions can allow us to address precision questions regarding SRCs. These include detailed study of the $|t|$ and kinematical dependencies of the reaction mechanisms necessary to fully establish plane-wave factorization. We can further extend measurements with this luminosity to search for and characterize exclusive 3N-SRC breakup in kinematic regions distinct from electron-scattering measurements. Finally, a high-luminosity measurement will allow us to search for rare channels like $J/\psi$ photoproduction, the measurement of which would allow the first insights into the high-$x$ gluonic structure of the nucleus and of the gluonic structure of SRC nucleons in particular.

We request 100 PAC days at Hall D using the GlueX detector with a 12 GeV electron beam energy and a $^4$He target, using a coherent peak energy of 8 GeV.

# Contents

# 1 Introduction

Short-range correlations (SRCs) are pairs of nucleons with high relative and lower center-of-mass momentum, which compose a sizeable fraction of the nucleus and have significant impact on nuclear structure [1–3]. Much has been learned about SRCs in recent years; they have been found to account for approximately 20% of nucleons in medium to heavy nuclei, to be dominated by proton-neutron pairs [4–7], and to dominate the high-momentum tail of the nuclear wave function [4, 6, 8–19]. Evidence has also been found linking the abundance of SRCs in a nucleus to the modification of nucleons within the nucleus (the EMC effect).

Many of these recent results have come about from the measurement of semi-inclusive $(e, e'N)$ and exclusive $(e, e'NN)$ SRC breakup processes. SRC data from the JLab 6 GeV program contribute to many of the recent results [6, 9, 10, 20]. Improvements in theoretical understanding and modeling of SRCs have also allowed us to better interpret SRC breakup data, but have been reliant on basic assumptions about the reaction mechanisms involved in SRC measurements [8, 15, 21, 22]. The 6 GeV data, being both of low statistics and limited purely to quasi-elastic electron-scattering, has been insufficient to guide and constrain these theories as they are developed.

More recently, measurements from the JLab 12 GeV program have sought to better establish the foundations of our theoretical understanding of SRCs. These experiments have included high-statistics measurements of $(e, e')$, $(e, e'N)$, and $(e, e'NN)$ over a wide range of nuclei in order to provide precision tests of the reaction mechanisms involved in electron-scattering, to gain insight into the details of the $NN$ interaction and nuclear wave function at short distances, and to search for and characterize Three-Nucleon (3N) SRCs [23].

Recently, a small sample of nuclear data has been measured using the real photon beam of Hall D incident on $^2$H, $^4$He,and $^{12}$C targets [24]. These data have enabled the first measurements of SRC breakup using quasi-elastic photoproduction channels such as $A(\gamma, \rho^- pp)$. Along with similar data measured using hadron-scattering [18,19], these measurements have enabled basic tests of universality of SRC properties between different probes and hard reactions. However, these data remain at a similar statistical precision to the 6 GeV data, and are insufficient for providing truly high-precision measurements of SRC properties. In order to provide precision data matching theoretical advances and other experimental data, it is necessary to take high-statistics photo-nuclear measurements of SRCs.

High-luminosity photo-nuclear data can also provide access to events such as incoherent $J/\psi$ photoproduction, which has a relatively low cross section at JLab energies. $J/\psi$ production at JLab has enabled measurement of the gluonic structure of the proton at high-$x$, in the threshold region for photoproduction [25, 26]. Measurements of incoherent $J/\psi$ photoproduction from nuclei have been performed by looking at data from Ultra-Peripheral Collisions at RHIC and the LHC [27–29], but these data are statistically limited and probe much lower values of $x$ than photoproduction measurements at JLab. A precision measurements of incoherent $J/\psi$ production from nuclei with photon energies between 6 and 12 GeV would be the first such measurement in the threshold region, and would extend to being the first measurement of sub-threshold photoproduction of $J/\psi$. These measurements can provide the first insights into the gluonic structure of nuclei and bound nucleons at high-$x$. Such a measurement is a necessary complement to measurements of the EMC effect, which show evidence for the modification of quarks in bound nucleons in the region $0.3 < x < 0.7$ [30]. Measurement of $J/\psi$ from nuclei near and below threshold can give the first constraints on the distributions of gluons within nuclei at similar values of $x$. Furthermore, the quasi-exclusive nature of incoherent $(\gamma, J/\psi\ p)$ photoproduction allows reconstruction of the initial proton involved in the reaction, allowing for direct testing of the differences between $J/\psi$ photoproduction on mean-field and SRC nucleons.

We propose here a 100-PAC day measurement of the nuclear target $^4$He, using the Hall D real photon beam with a coherent peak energy of 8 GeV and the GlueX detector in its standard configuration. The experiment has three primary goals:

1. High-precision study of reaction mechanisms of SRC breakup, particularly studying the resolution-dependence of the reaction by varying the momentum transfer $|t|$

2. Searches for exclusive 3N-SRC breakup in kinematics inaccessible to electron-scattering measurements

3. Measurements of incoherent $J/\psi$ photoproduction from nuclei, including sub-threshold production and production from SRC nucleons

We present an overview of the recent experimental and theoretical results in SRC studies in Section 2. In Section 3, we outline the primary physics goals of this experiments, and in Section 4, we detail the proposed experiment, including kinematics of the measurement, optimization of the coherent peak of photon energy, and expected rates for the channels of interest.

# 2 Recent Results

The study of short-range correlations is a broad subject. It covers a large body of experimental and theoretical work, as well as phenomenological studies of the implications of SRCs for various phenomena in nuclear, particle and astro-physics. The discussion below is focused primarily on recent experimental activities co-led by the spokespersons, and theoretical developments that are most relevant for the objectives of the current proposal. A full discussion of SRC physics is available in a recent RMP review [31], as well as in a theory-oriented review [3].

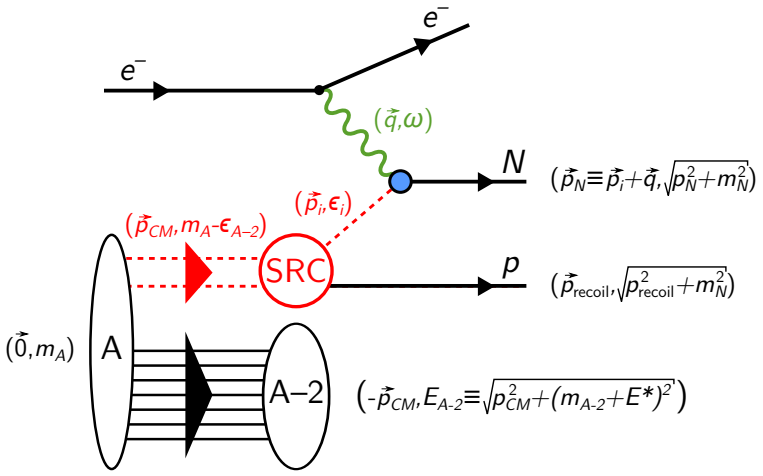


Figure 1: Diagrammatic representation and kinematics of the triple-coincidence $A(e,e'Np)$ reaction within the SRC breakup model. Dashed red lines represent off-shell particles. Open ovals represent undetected systems. Solid black lines represent detected particles. The momentum and energy of the particles are also indicated.

Previous studies of SRCs have used measurements of Quasi-Elastic (QE) electron scattering at large momentum-transfer, see Fig. 1. Within the single-photon exchange approximation, electrons scatter from the nucleus by transferring a virtual photon carrying momentum $\vec{q}$ and energy $\omega$. In the one-body view of QE scattering, the virtual photon is absorbed by a single off-shell nucleon with initial energy $\epsilon_i$ and momentum $\vec{p}_i$. If the nucleon does not re-interact as it leaves the nucleus, it will emerge with momentum $\vec{p}_N = \vec{p}_i + \vec{q}$ and energy $E_N = \sqrt{p_N^2 + m_N^2}$. Thus, we can approximate the initial momentum and energy of that nucleon using the measured missing momentum, $\vec{p}_i \approx \vec{p}_{\rm miss} \equiv \vec{p}_N - \vec{q}$, and missing energy, $\epsilon_i \approx m_N - \epsilon_{\rm miss} \equiv \epsilon_N - \omega$. When $\vec{p}_{\rm miss} > k_F$, the knockout nucleon is expected to be part of an SRC pair [2,3,5,6,18,31,32]. The knockout of one nucleon from the pair should therefore be accompanied by the simultaneous emission of the second (recoil) nucleon with momentum $\vec{p}_{\rm recoil} \approx -\vec{p}_{\rm miss}$. At the relevant high-$Q^2$ of our measurements ($> 1.7$–$2.0$ GeV/$c$), the differential $A(e,e'p)$ cross-sections can be approximately factorized as [33,34]:

$$\frac{d^6\sigma}{d\Omega_{k'}\,d\epsilon_{k'}\,d\Omega_N\,d\epsilon_N} = p_N\epsilon_N \cdot \sigma_{ep} \cdot \mathcal{S}(p_i,\epsilon_i), \tag{1}$$

where $k' = (k', \epsilon_{k'})$ is the final electron four-momentum, $\sigma_{ep}$ is the off-shell electron-nucleon cross-section [34], and $\mathcal{S}(p_i,\epsilon_i)$ is the nuclear spectral function that defines the probability for finding a nucleon in the nucleus with momentum $p_i$ and energy $\epsilon_i$. Different models of the $NN$ interaction can produce different spectral functions that lead to different cross-sections. Therefore, exclusive nucleon knockout cross-sections analyzed with this method are sensitive to the $NN$ interaction.

In the case of two-nucleon knockout reactions, the cross-section can be factorized in a similar manner to Eq. 1 by replacing the single-nucleon spectral function with the two-nucleon decay function

$\mathcal{D}_A(p_i, p_{\text{recoil}}, \epsilon_{\text{recoil}})$ [1,2,18]. The latter represents the probability for a hard knockout of a nucleon with initial momentum $\vec{p}_i$, followed by the emission of a recoil nucleon with momentum $\vec{p}_{\text{recoil}}$. $\epsilon_{\text{recoil}}$ is the energy of the $A-1$ system, composed of the recoil nucleon and residual $A-2$ nucleus.

Non-QE reaction mechanisms that add coherently to the measured cross-section can lead to high-$p_{\text{miss}}$ final states that are not due to the knockout of nucleons from SRC pairs, thus breaking the factorization shown in Eq. 1. To address this, the measurements discussed here are carried out at anti-parallel kinematics with $p_{\text{miss}} \geq 300$ MeV/$c$, $Q^2 \equiv q^2 - \omega^2 \geq 1.7$ (GeV/$c$)$^2$, and $x_B \equiv Q^2/2m_N\omega \geq 1.2$, where such non-QE reaction mechanisms were shown to be suppressed [2,3,31,32, 35,36].

For completeness, we note that from a theoretical standpoint, the reaction diagram shown in Fig. 1 can be viewed as a 'high-resolution' starting point for a unitary-transformed calculation [37]. Such calculations would soften the input $NN$ interactions and turn the electron scattering operators from one-body to many-body. This 'unitary-freedom' does not impact cross-section calculations but does make the extracted properties of the nuclear ground-state wave-function (e.g. the spectral function) depend on the assumed interaction operator. This discussion focuses on the high-resolution electron interaction model of Fig. 1, as it constitutes the simplest reaction picture that is consistent with both the measured observables [2, 3, 31, 32] and various reaction and ground-state ab-initio calculations [38].

### 2.1 Short-Distance $NN$ Interaction and the Generalized Contact Formalism

Precision SRC studies are only feasible if one has the ability to quantitatively relate experimental observables to theoretical calculations, ideally ones starting from the fundamental $NN$ interaction and accounting for all relevant reaction mechanisms. This is a challenging endeavor, as un-factorized ab-initio calculations of high-$Q^2$ nucleon knockout cross-sections are currently unfeasible for $A > 3$ nuclei. Even the simple factorized approximation of Eq. 1 requires knowledge of the nuclear spectral function that, at the moment, cannot be calculated using ab-initio techniques for high-momentum states in finite nuclei [38].

To help overcome this challenge, Generalized Contact Formalism (GCF), a factorized effective theory, was recently developed [21, 22, 39], which allows the calculation of factorized cross-sections, within a scale-separated approximation using the underlying $NN$ interaction as input [7,39]. This is done by providing a factorized model of the short-distance / high-momentum part of the many-body nuclear wave function leveraging the separation between the energy scales of the $A-2$ system (low energy) and the SRC pair (medium energy). Considering a high-$Q^2$ scattering reactions such as in Fig. 1 adds a third energy scale of the virtual photon (high-energy) that justifies the factorized approximation of Eq. 1.

The GCF provides a consistent model for nuclear two-body momentum distribution at high-momenta and at short-distance, as well as for two-body continuum states of the nuclear spectral and decay functions. Recent studies of the GCF:

- Demonstrated its ability to reproduce many-body ab-initio calculated nucleon momentum distributions in nuclei from $^4$He to $^{40}$Ca, above $k_F$, to $\approx 10\%$ accuracy [22];
- Extracted consistent SRC abundances (i.e., nuclear contacts) from ab-initio calculations of two-nucleon distributions in both coordinate and momentum space and from experimental data [22]; and
- Derived a new factorized expression for the nuclear correlation function with implications for calculations of double beta decay matrix elements [40] and demonstrated its relation to single-nucleon charge distribution measurements [41].

The main application of the GCF germane to this proposal is the modeling of the nuclear spectral and decay functions [39], allowing calculations of nucleon knockout cross-sections. For example, using Eq. 1 and the reaction model of Fig. 1, the $A(e,e'NN)$ cross-section can be expressed within the GCF as [7]:

$$\frac{d^8\sigma}{dQ^2 dx_B d\phi_k d^3\vec{p}_{CM} d\Omega_{\rm recoil}} = K \cdot \sigma_{eN} \cdot n(\vec{p}_{CM}) \cdot \left[ \sum_\alpha C_\alpha \cdot |\tilde{\varphi}^\alpha(|\vec{p}_{CM} - 2\vec{p}_{\rm recoil}|)|^2 \right], \qquad (2)$$

where subscripts '$N$' and 'recoil' stand for the leading and recoil nucleon respectively, $K$ is a kinematic term, (detailed in Ref. [7]), $\sigma_{eN}$ is the off-shell electron-nucleon cross-section, and $\alpha$ represents the spin and isospin quantum numbers of SRC pairs. $\tilde{\varphi}^\alpha$, $n(\vec{p}_{CM})$, and $C_\alpha$ respectively describe the relative motion, CM motion, and abundances of SRC pairs with quantum numbers $\alpha$. The functions $\tilde{\varphi}^\alpha$ are universal SRC pair relative momentum distributions, obtained by solving the zero-energy two-body Schrödinger equation of an $NN$ pair in quantum state $\alpha$ using an input $NN$ potential model. $n(\vec{p}_{CM})$ is the SRC pair CM momentum distribution, given by a three-dimensional Gaussian with width of $150 \pm 20$ MeV/$c$ [42–44]. $C_\alpha$ are the nuclear contact terms that determine the relative abundance of SRC pairs in quantum state $\alpha$. These are obtained through the analysis of ab-initio many-body calculations of two-nucleon densities [21, 22, 45].

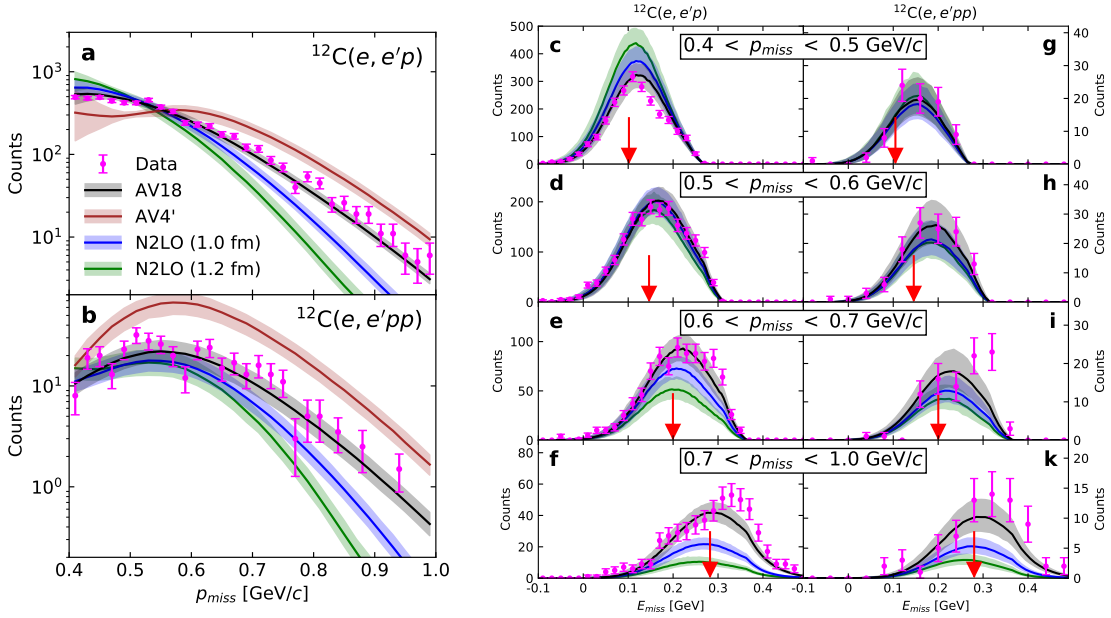


Figure 2: Left panel: the $p_{\rm miss}$ dependence of the $^{12}{\rm C}(e,e'p)$ (top) and $^{12}{\rm C}(e,e'pp)$ (bottom) event yields. Points show the measured data. Bands show the GCF calculations using the N2LO(1.0fm) (blue) and AV18 (black) interactions. Right panel: the $\epsilon_{\rm miss}$ dependence of the $^{12}{\rm C}(e,e'p)$ (left column) and $^{12}{\rm C}(e,e'pp)$ (right column) event yields in four different ranges of $p_{\rm miss}$. The purple arrow indicates the expected $\epsilon_{\rm miss}$ for standing SRC pair breakup with a missing-momentum that is equal to the mean value of the data.

Since its development, GCF has been compared to data from a range of experiments [7, 8, 19, 46, 47], validating and aiding the interpretation of those results. In Figs. 2 and 3 we showcase the extensive results from Ref. [8], where Eq. 2 is used to calculate the individual $(e,e'p)$ and $(e,e'pp)$ cross-sections in the kinematics of our SRC measurements. The calculation was done using two $NN$ interaction models to obtain $\tilde{\varphi}^\alpha$: the phenomenological AV18 [48], and Chiral EFT-based

local N2LO(1.0 fm) [49]. Nuclear contacts $C_\alpha$ and width of the CM momentum distribution were obtained from theoretical calculations [21, 22, 43–45] and nuclear transparency and single-charge exchange reaction effects were accounted for as detailed in the online supplementary materials of Ref. [7], using the calculations of Ref. [35]. The model systematic uncertainty is determined from the uncertainties in the GCF input parameters and reaction effects correction factors.

The left panel of Fig. 2 shows the $p_{\rm miss}$ dependence of the measured and GCF-calculated $^{12}$C$(e,e'pp)$ and $^{12}$C$(e,e'p)$ event yields for the two interactions. The AV18 interaction is observed to describe both $(e,e'p)$ and $(e,e'pp)$ data over the entire measured $p_{\rm miss}$ range. The N2LO(1.0 fm) interaction agrees with the data up to its cutoff and, as expected, decreases exponentially above it.

The right panel of Fig. 2 shows the $\epsilon_{\rm miss}$-$p_{\rm miss}$ correlation for the $^{12}$C$(e,e'pp)$ and $^{12}$C$(e,e'p)$ reactions. The average value of $m_N - \epsilon_1$ is observed to increase with $p_{\rm miss}$, peaking at the expected value for the breakup of a standing SRC pair (indicated by the purple arrows) for both reactions. The GCF calculations follow the same trend. However, the AV18 interaction agrees with the data over the entire $\epsilon_{\rm miss}$-$p_{\rm miss}$ range, while the chiral interactions under predict at the highest $p_{\rm miss}$.

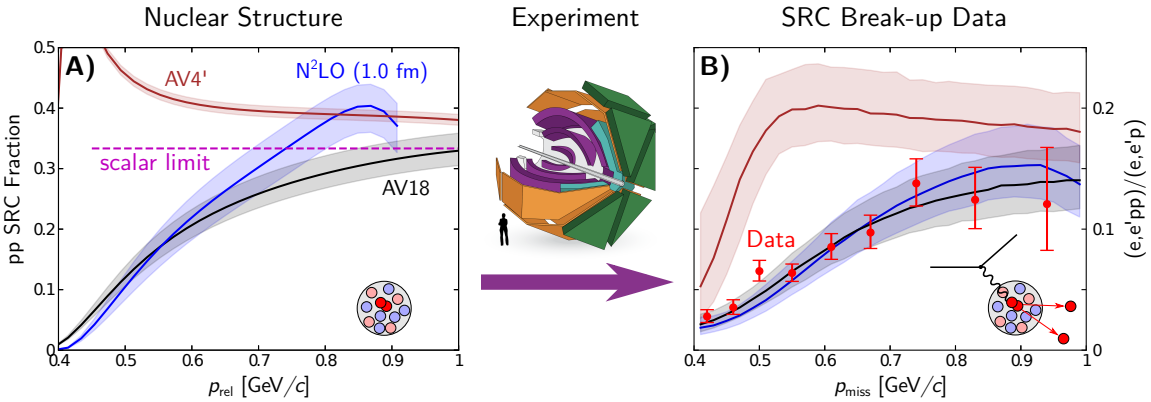


Figure 3: A: the $pp$ pair fraction in $^{12}$C as predicted by GCF using AV18, AV4', and Chiral N2LO(1.0 fm) interactions. B: the ratio of $^{12}$C$(e,e'pp)$ to $^{12}$C$(e,e'p)$ event yields for data (red points) and GCF (bands), including all experimental effects. Both the AV18 and N2LO(1.0 fm) interactions are consistent with data, and show an increase from a tensor-dominated regime at $p_{\rm miss} = 0.4$ GeV/$c$ to scalar spin-independent regime approaching $p_{\rm miss} = 1$ GeV/$c$. The AV4' interaction, which has no tensor component, leads to predictions that are inconsistent with data.

Fig. 3 considers the $^{12}$C$(e,e'pp)/^{12}$C$(e,e'p)$ yield ratio, a measure of the impact of the tensor force in the $NN$ interaction. In this figure, the AV18 and the chiral N2LO(1.0 fm) interactions are compared to the AV4′ interaction, which does not include a tensor force. The right panel shows the data yield ratio as well as the GCF-calculated yield ratio. Both the data, and the calculations with the AV18 and N2LO(1.0 fm) interactions show the $pp$ fraction increasing with $p_{\rm miss}$, consistent with a transition from tensor- to scalar-dominated regions of the interaction [5]. By contrast, the calculation with the AV4′ interaction over-predicts the fraction of $pp$ pairs observed in the data.

The left panel shows the fraction of $pp$ pairs in $^{12}$C as predicted by the GCF formalism as a function of $p_{\rm rel.} \equiv \frac{1}{2}|\vec{p}_{\rm miss} - \vec{p}_{\rm recoil}|$. The AV18 and N2LO(1.0 fm) interactions approach limit predicted by a purely spin-independent interaction. The AV4′ interaction, without a tensor force, predicts a $pp$ fraction above this scalar limit.

We note that our confidence in these results is supported by the fact that the GCF-based calculations describe well numerous other measured kinematical distributions in both this experiment and others. Two examples are shown in Fig. 4. On the left, the missing energy distribution for $^4$He$(e,e'p)$ data measured in SRC kinematics in Hall A with a small acceptance spectrometer [5] are compared to GCF calculations [46], which are able to reproduce the measured distribution. On

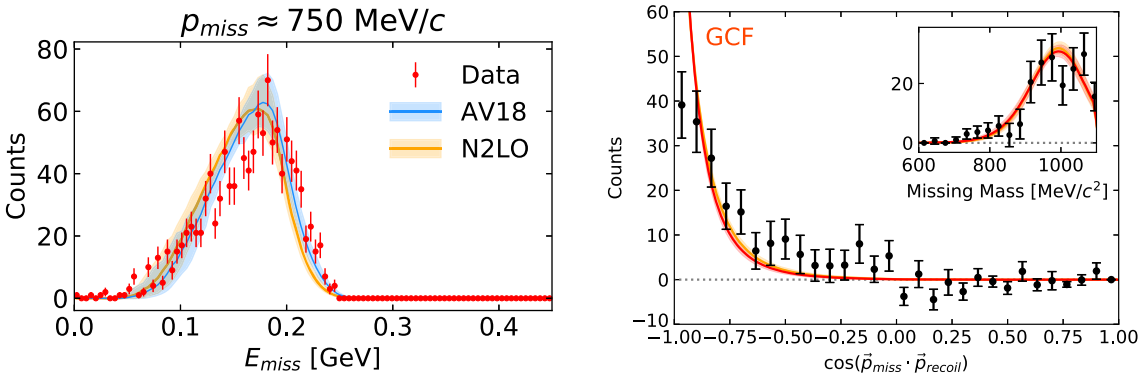


Figure 4: Examples of the agreement between GCF calculations and experimental data. Left: The missing energy distribution for $^4$He$(e,e'p)$ events measured in Hall A, with a high-resolution, small acceptance spectrometer (taken from Ref. [46]). Right: The distribution of angles between the missing momentum, $\vec{p}_{\rm miss}$ and recoil nucleon momentum, $\vec{p}_{\rm recoil}$, along with the missing mass distribution (inset) for C$(e,e'pn)$ events measured over a wide acceptance by CLAS (taken from Ref. [47]).

the right are shown distributions for the angle between the missing momentm and recoil momentum and for the reconstructed missing mass (inset) of $C(e,e'pn)$ events measured by CLAS over a wide acceptance [47]. Again, GCF is able to reproduce the measured distributions.

Thus, the results presented here showcase the use of high-$Q^2$ electron scattering data to quantitatively study the nuclear interaction at very large momenta. It is interesting to note that for the AV18 interaction, we observe good agreement with the data up to 1 GeV/$c$, which corresponds to SRC configurations with nucleons separated by a distance smaller than their radii [50]. As discussed below, previous studies indicated that in such extreme conditions the internal quark-gluon structure of SRC nucleons can well be modified as compared with that of free nucleons [9, 31, 51–53]. The ability of the AV18-based GCF calculation to reproduce our data over the entire measured $\epsilon_{\rm miss}$-$p_{\rm miss}$ range suggests that such modifications do not significantly impact the effective modeling of the nuclear interaction, offering support for using point-like nucleons as effective degrees of freedom for modeling of nuclear systems up to very high densities.

## 2.2 Two-Nucleon Knockout Reactions

The above-mentioned results constitute some of the most advanced analyses that employ the scale-separated GCF to calculate factorized nucleon-knockout cross-sections using different models of the $NN$ interaction. These studies are made possible by the vast progress made in the study of SRCs using hard knockout reactions over the last decade. Below, we review key published results from initial measurements of nuclei from $^4$He to $^{208}$Pb.

### 2.2.1 $np$-SRC dominance and the tensor interaction

First measurements of exclusive SRC pair breakup reactions focused primarily on probing the isospin structure of SRC pairs. These experiments were initially done at BNL using hadronic (proton) probes on $^{12}$C, and continued at JLab with leptonic (electron) probes on $^4$He, $^{12}$C, $^{27}$Al, $^{56}$Fe and $^{208}$Pb.

Focusing on a missing momentum range of 300–600 MeV/$c$, comparisons of the measured $A(e,e'p)$ and $A(e,e'pN)$ cross-section indicated that the full single-proton knockout cross-section is exhausted by the two-nucleon knockout cross-sections, i.e., the data were consistent with every $(e,e'p)$ event having the correlated emission of a recoil nucleon [5–7,18]. A common interpretation of these results

is that the nucleon momentum distribution above $k_F$ is dominated by nucleons that are members of SRC pairs.

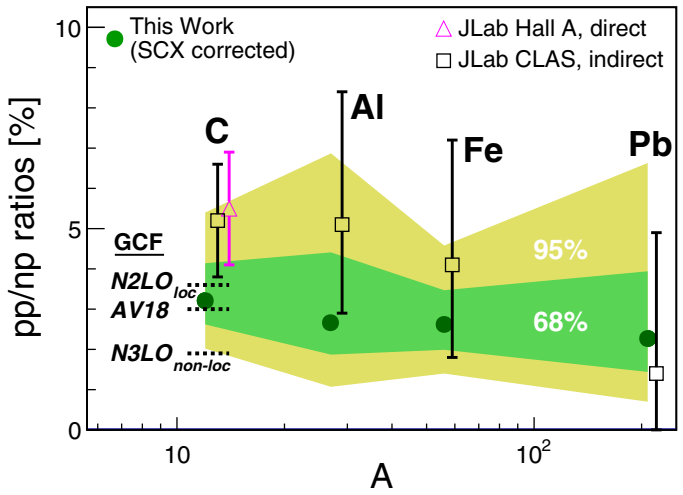


Figure 5: $np$-SRC dominance in nuclei from $^{12}$C to $^{208}$Pb extracted from $A(e,e'Np)$ and $A(e,e'p)$ measurements [6,7,20], compared with GCF calculations [7].

Furthermore, the measured $A(e,e'pn)$ and $A(e,e'np)$ cross-sections were found to be significantly higher than the $A(e,e'pp)$ cross-section. This finding, consistently observed in all measured nuclei, was interpreted as evidence for $np$-SRC pairs being about 20× more abundant than $pp$-SRC pairs (Fig. 5). From a theoretical standpoint, this $np$-SRC predominance was interpreted as resulting from the dominance of the tensor part of the $NN$ interaction at the probed sub-fm distances [3,31,54–56] (see Fig. 6.

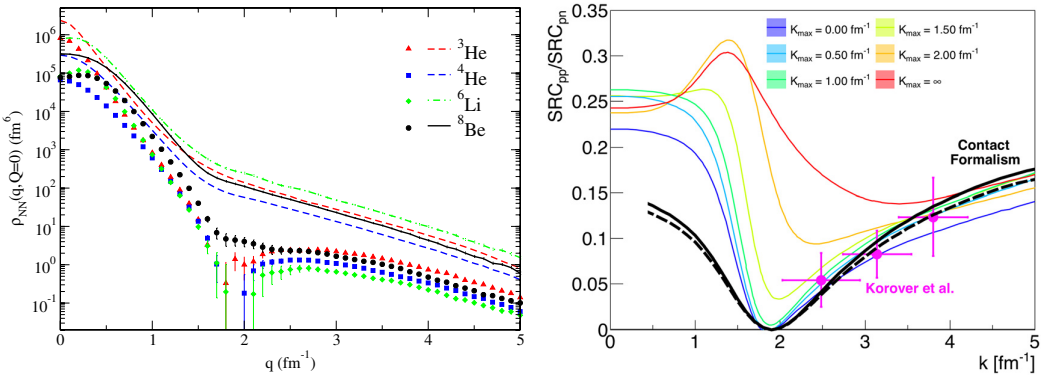


Figure 6: Left: calculated $pp$ (points) and $np$ (lines) stationary pair momentum densities in light nuclei [54]. Right: measured and calculated $^4$He $pp/np$ pair density ratios as a function of the pair relative momentum [22].

It should be pointed out that, on average, the tensor part of the $NN$ interaction is long-ranged and small compared to the dominant scalar part. However, studies of the deuteron suggest that its second order effect, viewed as a two-pion exchange term, becomes important in the momentum range where the scalar force approaches zero ($\approx$ 0.75–1 fm) [31]. At shorter distances, i.e., higher relative momenta, the dominance of the tensor interaction is expected to be washed out, which would manifest in an increase in the fraction of $pp$-SRC pairs with much larger missing momentum. Fig. 6

shows the measured increase in the fraction of *pp*-SRC pairs [5], which is overall consistent with theoretical expectation based on calculations of two-nucleon momentum distributions [45] and their GCF representation [22]. The large error bars of the $^4$He data made it hard to draw any conclusive quantitative conclusions on the evolution of the $NN$ interaction beyond the tensor-dominated regime. However, as shown in Fig. 3, the combination of improved data, and recent theoretical developments (such as the GCF), has made studying these extreme limits possible [8, 47].

### 2.2.2 SRC pair C.M. motion

Measurements of exclusive two-nucleon knockout reactions allow us to probe the detailed characteristics of SRC pairs, going beyond their isospin structure. One such property of interest is the C.M. motion of SRC pairs. It is a measure of the interaction of the pair with the 'mean-field' potential created by the residual $A-2$ system. Its magnitude, as compared with the relative motion of the nucleons in the pairs, is key for establishing effective scale-separated models of SRCs such as the GCF presented above and serves as an input for theoretical calculations.

The CM motion of SRC pairs is expected to be described by a Gaussian distribution, defined by its width. Therefore, experiments often report on their extraction of the C.M. Gaussian width, $\sigma_{CM}$.

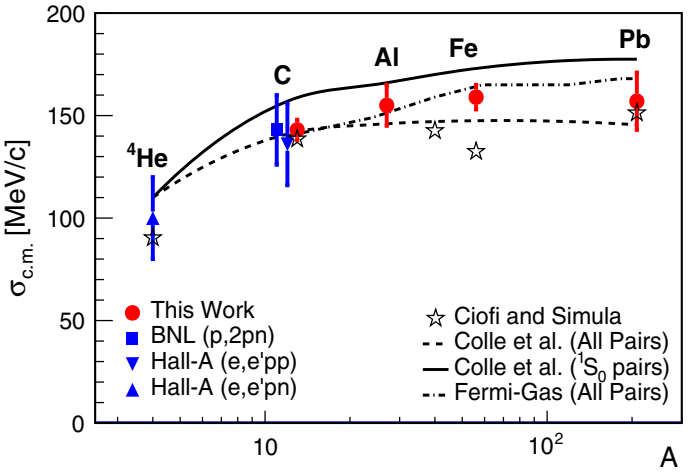


Figure 7: Width of *pp*-SRC pairs C.M. momentum distribution, extracted from $A(e,e'pp)$ data (red circles) [42], compared with previous extractions (blue points). The width is extracted assuming a 3D Gaussian for the C.M. distribution, defined by its width, $\sigma_{CM}$. The lines and stars show mean-field theory predictions [43, 44].

Fig. 7 shows the latest results from the extraction of the $\sigma_{CM}$ for pp-SRC pairs from an analysis of $A(e,e'pp)$ data [42]. The extracted C.M. momentum distribution for the measured nuclei was observed to be consistent with a Gaussian distribution in each direction, as expected. The extracted values of $\sigma_{CM}$ were observed to vary between 140 and 160 MeV/$c$, and are consistent with a constant within experimental uncertainties.

Comparisons with theory predictions show good agreement with either a simple Fermi-gas model prediction (where the $NN$ pairs are formed from two randomly chosen nucleons, each following a Fermi-Gas momentum distribution with $k_F = 250$ MeV/$c$) or more realistic mean-field calculations [43, 44]. Interestingly, the data seem to be higher than the mean-field predictions that assume all $NN$ pairs can form SRC pairs, but lower than the most restrictive $^1$S$_0$ calculation (i.e., assuming only mean-field *pp* pairs in a relative $^1$S$_0$ state can form *pp*-SRC pairs). This indicates some selectivity in the SRC pair formation process and was suggested to provide insight to their quantum

numbers [42, 44, 57].

## 2.3 Final State Interactions in Hard QE Scattering

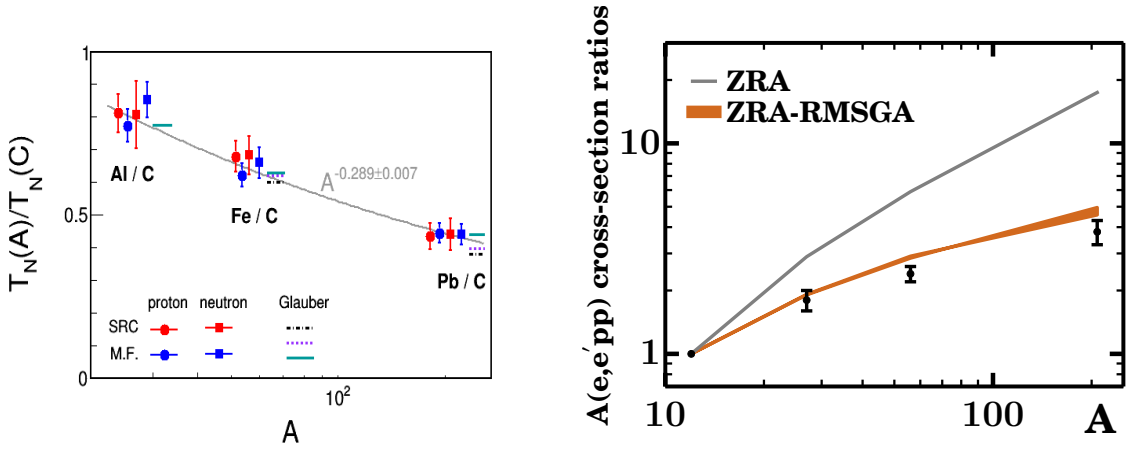


Figure 8: Nucleon transparency ratios for nuclei relative to $^{12}$C, extracted from single-nucleon knockout measurements (left) [58], and calculations of the two-nucleon knockout reaction [57] using Glauber theory (right).

The results presented above in sections 2.1 and 2.2 require corrections for reaction effects such as final-state interactions (FSI) and singe-charge exchange (SCX). Therefore, understanding the impact of such reaction mechanism effects on hard electron QE scattering cross-sections is crucial for the interpretation of measurements in general, and specifically their relation to ground-state properties of nuclei. In high-$Q^2$ reactions, one may use the Generalized Eikonal approximation within a Glauber-framework to perform quantitative estimations of reaction effects such as FSI and SCX. However, additional experimental verification of this approach in the kinematics of our measurements are needed. Several measurements of the nuclear transparency of proton knockout in $(e, e'p)$ and $(e, e'pp)$ reactions in SRC kinematics were compared them with theoretical calculations using the Glauber approximation [11,57] (Fig. 8, right). The experimentally extracted transparency ratios showed good agreement with Glauber calculations. Recently, this work was extended to measurements of neutron knockout $(e, e'n)$ reactions in both SRC and Mean-Field kinematics [58] (Fig. 7 top panel). The extracted transparency for both proton and neutron knockout in mean-field and SRC kinematics were observed to agree with each other and with Glauber calculations. The combined nuclear mass dependence of the data is consistent with power-law scaling of $A^\alpha$ with $\alpha = -0.285 \pm 0.011$, which is consistent with nuclear surface dominance of the reactions.

## 2.4 Reaction Mechanisms Uncertainties in the Interpretation of SRCs

The results described above are almost all derived from electron scattering measurements, with only a single proton scattering C$(p, ppn)$ measurement [4]. Thus, the interpretation of these experimental results relies on an assumed electron interaction mechanism at large momentum transfers. There are a number of different electron-scattering reaction mechanisms that can lead to two-nucleon emission (see Fig. 9). While the experiments described above have been performed at kinematics where many of these effects have been minimized, there are still interpretational uncertainties due to these other possible reaction mechanisms. These reaction mechanisms are not present or are very different for proton scattering.

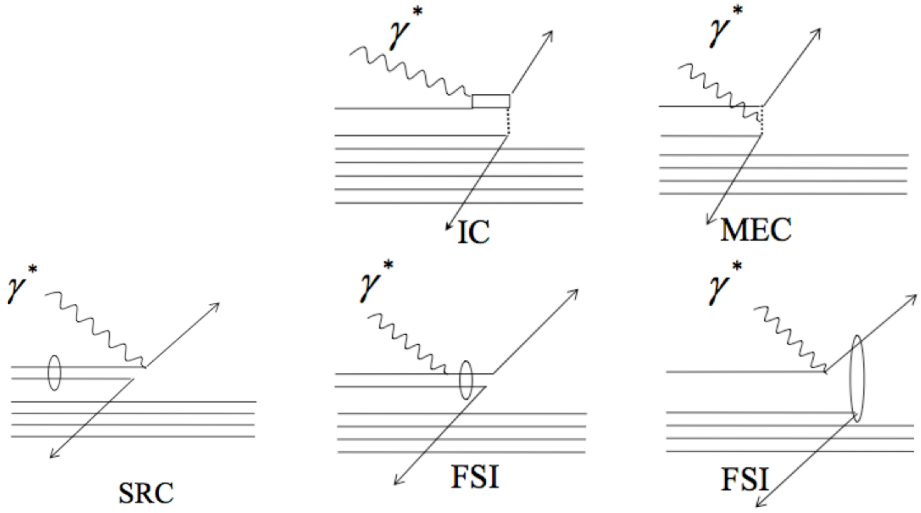


Figure 9: The reaction mechanisms for electron-induced two nucleon knockout. The virtual photon can be absorbed on one nucleon of an SRC pair, leading to the emission of both nucleons (SRC). The virtual photon can excite a nucleon to a $\Delta$, which deexcite by exchanging a pion, resulting in the emission of two nucleons (IC). The virtual photon can be absorbed on a pion-in-flight (MEC). The virtual photon can be absorbed on one nucleon of an SRC pair which rescatters from the other nucleon in the pair (FSI (left)). The virtual photon can be absorbed on an uncorrelated nucleon which rescatters from another nucleon (FSI (right)).

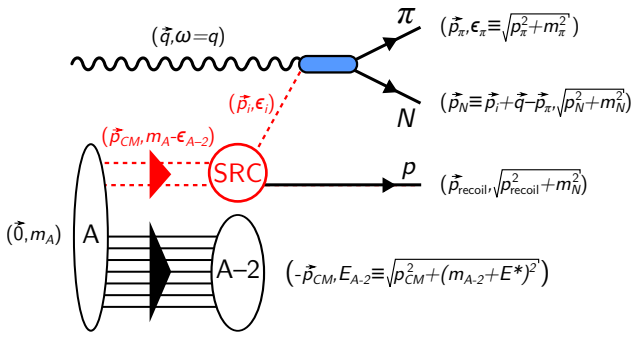


Figure 10: Diagrammatic representation and kinematics of the triple-coincidence $A(\gamma,\pi Np)$ reaction, one of the main channels of interest for SRC breakup by a real photon beam. As in Fig. 1, dashed red lines represent off-shell particles. Open ovals represent un-detected systems. Solid black lines represent detected particles. The momentum and energy of the particles are also indicated.

Photon scattering will also proceed through very different reaction mechanisms. Instead of quasielastic nucleon knockout, the primary photo-induced reaction studied here will be $\gamma n \to p\pi^-$, with a second nucleon (the correlated partner nucleon) emitted backward (see Fig. 10. For this reaction, the IC and MEC reaction mechanisms will be absent or significantly different. In addition, because the correlated partner nucleon will be emitted backwards, the effects of Final State Interactions (FSI) will also be quite different. It is much more difficult to produce backward nucleons that forward ones.

Thus photonuclear measurements of SRCs will provide a crucial reaction mechanism check for SRC studies.

## 2.5 SRC Universality

Much of our understanding of SRCs comes from electron scattering measurements. The interpretation of these experiments rests on assumptions about the mechanism of the reaction. In recent years, efforts have been made to decouple our understanding of the ground-state properties of SRCs from the specific electron-scattering measurements used to establish them. The factorized GCF cross section model has provided a framework for studying this, expressing the total cross section for SRC breakup events into the product of a ground-state nuclear spectral function and a single-body operator describing the hard reaction with the probe. This factorization may be tested using two approaches. First, we may test the resolution-dependence of this factorization by changing the momentum-transfer scale of the hard reaction, either $Q^2$ in electron-scattering or $|t|$ for other probes.. Second, we may compare the ability of the GCF to describe different types of hard reactions from correlated nucleons, comparing electron-scattering measurements to those using hadron- or photon-scattering.

### 2.5.1 Resolution-dependence

The resolution-dependence of quasi-elastic electron-scattering measurements has been studied in initial analysis of the Hall B Run Group M measurement E12-17-006 [59]. Fig. 11 shows an example of the ratio $^4\mathrm{He}(e,e'pp)/^4\mathrm{He}(e,e'p)$ for a fixed bin in $p_{miss}$, examined as a function of resolution $Q^2$. This observable is sensitive to the isospin structure of SRCs within the nucleus, and varies significantly as a function of $p_{miss}$, but GCF calculations predict a very weak dependence on $Q^2$ (largely an effect of the proton form factor). The data are seen to have a roughly constant value as a function of $Q^2$, with some possible deviation from this scaling at smaller $Q^2$. Some deviation from scaling at small momentum transfer is anticipated; the assumptions of the plane-wave impulse approximation are expected to be valid only at large momentum-transfer, and at small $Q^2$ contributions from MEC or other two-body operators are expected to come into play. As such, these preliminary results are largely consistent with the picture of SRC breakup reactions being a universal property of the nucleus rather than the reaction. Similar studies have not yet been possible for other measurements due to the limited statistics of such data.

### 2.5.2 Photon-Scattering

The probe-dependence of SRC-breakup measurements has been tested by a number of experiments which have measured SRCs using probes other than electrons. The Hall D SRC-CT experiment E12-19-003 [60] performed the first measurement of SRCs using high-energy photoproduction channels, with analysis currently being performed on $\rho^-$ and $\rho^0$ photoproduction from SRC nucleons. Fig. 12 shows preliminary results from the analysis of the exclusive SRC breakup channel $(\gamma, \rho^- pp)$. The left plot shows a measurement of the center-of-mass momentum of the SRC pair for each nucleus, compared with prediction from the GCF. In each case the center-of-mass motion for the pairs are generated using the values extracted from electron-scattering measurements (see Fig. 7). The GCF predictions do a good job of describing the measured data, and particularly capture the $A$-dependence

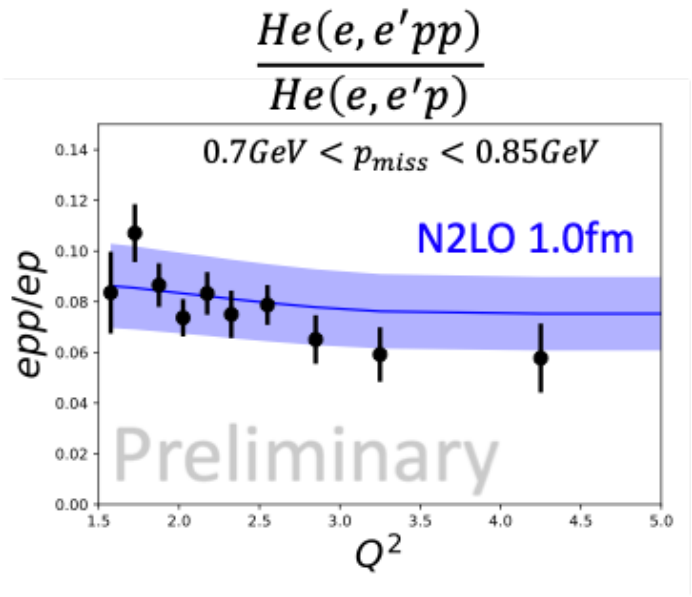


Figure 11: Measurement of the ratio $(e, e'pp)/(e, e'p)$ as a function of $Q^2$ for the range $0.7 < p_{miss} < 0.85$ GeV/$c$. The data can be seen to be largely independent of $Q^2$ and to agree with GCF predictions.

of this properties of the SRC pairs. The data seem to be slightly broader than GCF predictions for $^4$He and $^{12}$C, and it is currently being studied whether this is indicative of SRC properties or FSI rescattering.

Fig. 12 (right) shows measured distributions for the spectator proton in $(\gamma, \rho^- pp)$ events. These data are compared with GCF predictions using different models of the short-distance $NN$-interactions, with the phenomenological AV18 interaction in blue and the chiral N2LO interaction in green. Electron-scattering data have been shown to be sensitive to details of the $NN$-interaction at short range, and to agree well with AV18 predictions at high relative momentum. We find here that the AV18 predictions do a similarly good job of describing the data for $^2$H and $^4$He. The agreement with data for $^{12}$C is worse for AV18, but this is likely an effect of FSI; transport calculations of FSI using the GENIE model have calculated that the momentum for spectator nucleons is attenuated in medium-to-heavy nuclei such as $^{12}$C due to rescattering, a prediction which has been found to agree with electron-scattering measurements as well [61].

### 2.5.3 Hadron-Scattering

Hadronic probes with proton quasi-elastic scattering off nucleons in nuclei provide another "scheme" to probe SRCs. Taking advantage of the larger nuclear compared to electromagnetic cross section in electron scattering, the event rate increases by two orders of magnitude. In a conventional experimental setup, the beam proton hits a fixed nuclear target and knocks out a high-energy nucleon from an SRC pair and the nucleus. However, it is experimentally challenging to isolate the outgoing SRC nucleons with only a few hundred-MeV/c momenta while the scattered nucleons, including the beam proton, suffer strong final-state interactions (FSI) leading to distorted momenta. A novel approach that we implemented uses inverse kinematics in which the nucleus of interest forms the beam and scatters off a proton target. Thus, one can measure and distinguish all three high-momentum nucleons at different angles and reconstruct the 2N-SRC events. Additional detection of the ion fragments after the reaction, that travel with nearly beam velocity, enables us to identify the

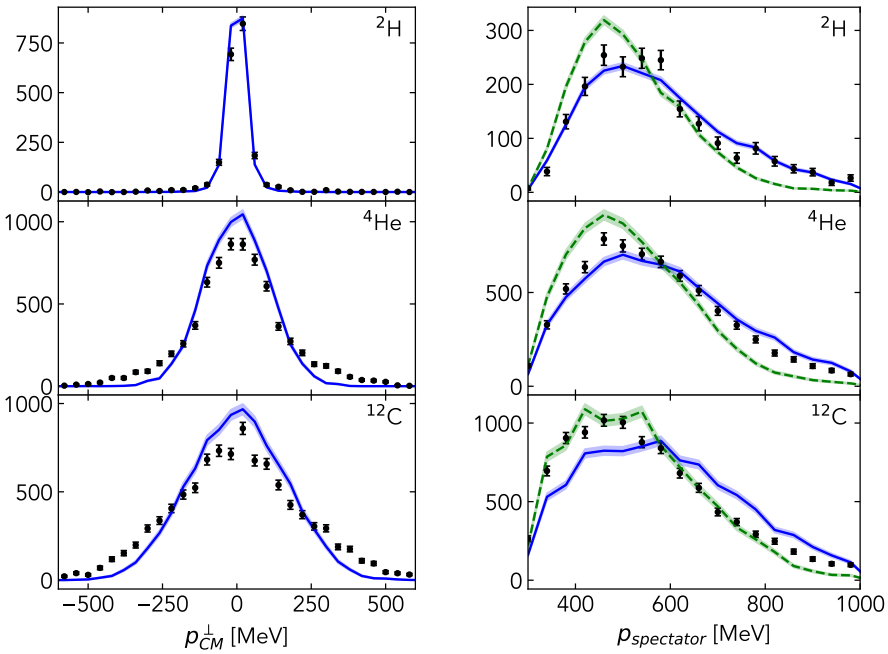


Figure 12: Preliminary results from the analysis of the exclusive SRC breakup channel $(\gamma, \rho^- pp)$. Data (black dots) are compared with GCF prediction for each nucleus, using the AV18 $NN$-interaction model (blue solid line) and the chiral N2LO interaction (green dashed line).

final state and largely suppress FSI, and thus gain direct access to observables to study SRC scale independence and universality. A pilot experiment at JINR using a 12C beam of 4 GeV/$c$/nucleon on a proton target [19] demonstrated the principle of the inverse kinematics to probe SRCs and opened a new research path to study SRCs, particularly in asymmetric nuclei. The quasi-free proton knockout on $^{12}$C with the coincident detection of $^{11}$B demonstrated the suppression of FSI and prove the extraction of the ground-state missing-momentum distribution of p-shell nucleons in $^{12}$C. Based on that, SRCs could be clearly identified for the first time in proton scattering in inverse kinematics, resulting in the identification of 23 pn-SRC and two pp-SRC pair break-ups with $^{10}$B and $^{10}$Be fragments, respectively, as shown in Fig. 13 [19].

Despite the limited statistics, the pair ratio reflects the np-pair dominance and is in full agreement with predictions based on ab-initio many-body calculations. In case of pair breakup and the quasi-free scattering assumption, the ion fragment carries the recoil momentum of the pair, which allows to infer the pair center-of-mass momentum directly from the measurement of the $A-2$ system in inverse kinematics. Done for the first time in this experiment, the obtained Gaussian momentum width (sigma) of $156\pm27$MeV/$c$ agrees well with previous, but only indirect extractions from electron scattering [42]. All the experimental results agree with previous electron scattering experiments and predictions within the GCF, underlining the universal access to SRCs also using proton probes.

As opposed to mean field nucleon knockout, where the $A-1$ system carries the recoil momentum, for SRC pairs the pair nucleon momenta balance each other which is reflected in the opening angle between the missing momentum and reconstructed nucleon recoil momentum. As shown in Fig. 14 (left), this distribution peaks towards 180° reflecting a back-to-back emission and confirming a strong correlation of the pair nucleons. In contrast, we find the first direct experimental evidence that the pair is scale separated from the rest of the nucleus by the uncorrelated opening angle between the

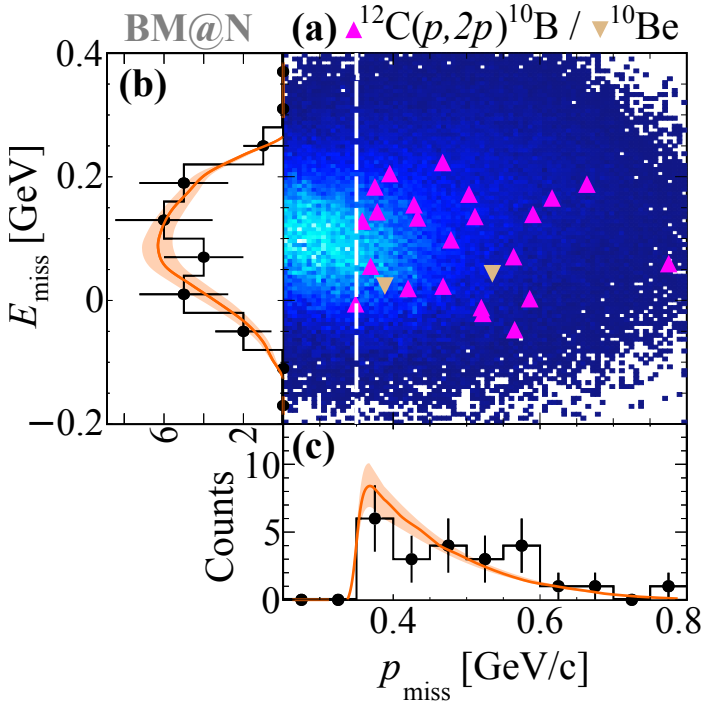


Figure 13: Correlation between the missing energy $E_{miss}$ and missing momentum $p_miss$ for the measured $^{12}$C$(p, 2p)^{10}$B (upwards-facing purple triangles) and $^{12}$C$(p, 2p)^{10}$Be (downwards-facing brown triangles) SRC events, on top of the GCF simulation (the colour scale is only relative as the absolute scale is set by the simulation statistics). The vertical white dashed line shows our event-selection cut of $p_{miss} > 350$MeV$/c$. Taken from Ref. [19]

$A-2$ momentum and the pair's relative momentum, Fig. 14 (right). This angular distribution is flat, unlike the previously mentioned nucleon-nucleon angle distribution. The results show a strongly correlated pair while it is only weakly correlated with the spectator nucleus. This supports one of the main assumptions in our understanding of SRCs and in theories like the GCF, namely a universal scale separation.

Following this pilot experiment, improved quantitative studies are being performed at JINR, and the first SRC experiment on a short-lived and extremely neutron-rich nucleus, namely $^{16}C$, has taken place at GSI-FAIR. Taking advantage of inverse kinematics, we can study SRC with radioactive-ion beams and for instance understand their dynamics in very asymmetric nuclear systems.

## 2.6 3N-SRC Searches

Experiments conducted at JLab measured the outgoing high-momentum nucleons from 2N-SRCs at intermediate relative momenta ($\gtrsim$ 400 MeV$/c$) and discovered that these 2N-SRC pairs are predominantly neutron-proton pairs with large relative momentum ($p_{rel} > k_F$) and smaller center-of-mass momentum ($p_{CM} \sim k_F$); see Fig. 15(a). Nucleons can also form close 3N-SRC clusters. Breaking up such a 3N-SRC cluster creates three fast-moving nucleons in different directions while their total center-of-mass momentum remains small, as shown in Fig. 15(b,c).

2N-SRC physics has been studied extensively over the last two decades using primarily electron-scattering where the nucleons from SRCs are probed with large momentum transfer in quasi-elastic (QE) scattering kinematics [12, 14, 20, 31]

Unlike 2N-SRC, the features and importance of 3N-SRC are mostly unknown. Given the proba-

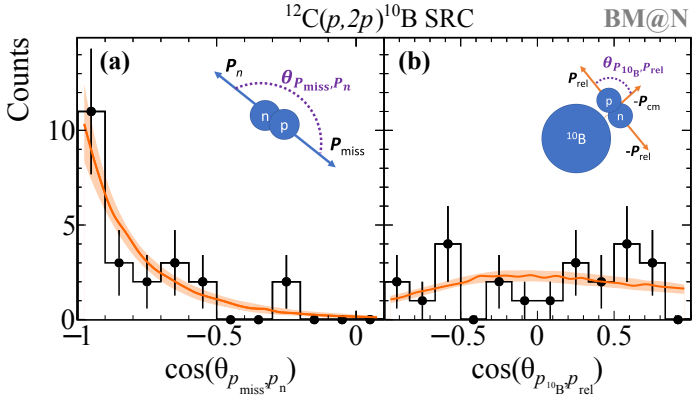


Figure 14: Correlation between the missing energy $E_{miss}$ and missing momentum $p_miss$ for the measured $^{12}$C$(p,2p)^{10}$B (upwards-facing purple triangles) and $^{12}$C$(p,2p)^{10}$Be (downwards-facing brown triangles) SRC events, on top of the GCF simulation (the colour scale is only relative as the absolute scale is set by the simulation statistics). The vertical white dashed line shows our event-selection cut of $p_{miss} > 350$MeV$/c$. Taken from Ref. [19]

bility of forming a 3N-SRC is significantly lower, a direct measurement of 3N-SRC in the $(e,e'pNN)$ reaction channel requires enormous luminosity and beam time.

The $(e,e')$ channel is the only electron-scattering reaction to effectively search for 3N-SRC by comparing QE cross-section ratios between heavy nuclei and $^3$He. If 3N-SRC appear in both nuclei, the cross section distribution of a nucleus $A$ would have the same shape as one of $^3$He, so their ratios should give a flat value in the $2 < x_B < 3$ region.

An early $(e,e')$ experiment in Hall B at JLab suggested a hint of 3N-SRC when measuring $^4$He and $^3$He cross-section ratios [13], but this was later shown to result from a bin-migration effect from the detector resolution. A later experiment in Hall C performed the same measurements at higher $Q^2$ [63] but the results were inconclusive due to the large uncertainties. A dedicated measurement in Hall A was performed to measure $^4$He and $^3$He ratios with high precision and found no indication of a 3N-SRC plateau [64], as shown in Fig. 16(a).

A recent reanalysis [65] of existing SLAC data and the Hall C data introduced a light-cone variable for 3-body interaction $(\alpha 3N)$ and claimed to be more sensitive to identifying the 3N-SRC scaling, seen in Fig. 16(b). The large errors in the claimed 3N-SRC region leave this claim inconclusive. The authors also suggested that a much higher four-momentum-transfer $Q^2$ is required to suppress FSI and separate 3N-SRC from fast-moving 2N-SRC pairs. However, the QE scattering cross section drops proportionally to $1/Q^4$, making high-precision measurements of 3N-SRC using $(e,e')$ at high $Q^2$ impossible. The precision study of 3N-SRC requires a different experimental technique.

## 2.7 The EMC Effect and SRCs

The relative abundance of SRC pairs in nuclei can be extracted from measurements of inclusive $(e,e')$ cross-section ratios for different nuclei at high-$Q^2$, $x_B > 1$ kinematics [2, 3, 9, 13, 31, 32, 63, 66, 67]. For fixed $Q^2$, these cross-section ratios scale as a function of $x_B$ starting approximately at $x_B \geq 1.5$ The height of the scaling plateau is often used to extract the relative number of high-momentum nucleons (i.e. SRC pairs) in the measured nuclei. We refer to these as the 'SRC scaling coefficients'.

In a recent series of publications [31, 68–70], we and others have shown that the extracted SRC scaling coefficients linearly correlate with the strength of the EMC effect in nuclei from $^3$He to $^{197}$Au. The latter is the slope of the deviation from unity of the isoscalar DIS cross-section ratio for nuclei relative to deuterium in the range $0.3 \leq x_B \leq 0.7$. The EMC effect is commonly interpreted as

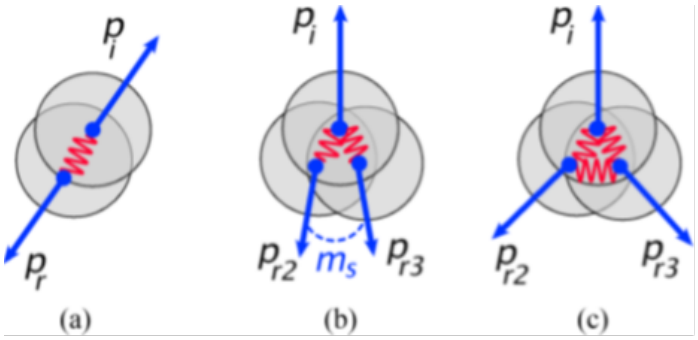


Figure 15: Schematic illustration of 2N-SRC and 3N-SRC structure [62]. Breaking up the 2N-SRC results in a back-to-back correlation of the pair shown in (a). Similarly, breakup up the 3N-SRC results in three nucleons with different momenta, but a small total momentum. Two extreme 3N-SRC configurations are: (b) two nucleons have similar and co-linear momentum while the third has twice the momentum in the opposite direction, or (c) three nucleons travel with equal momenta along different directions separated by an angle of 120°. Other configurations lie between these two extremes.

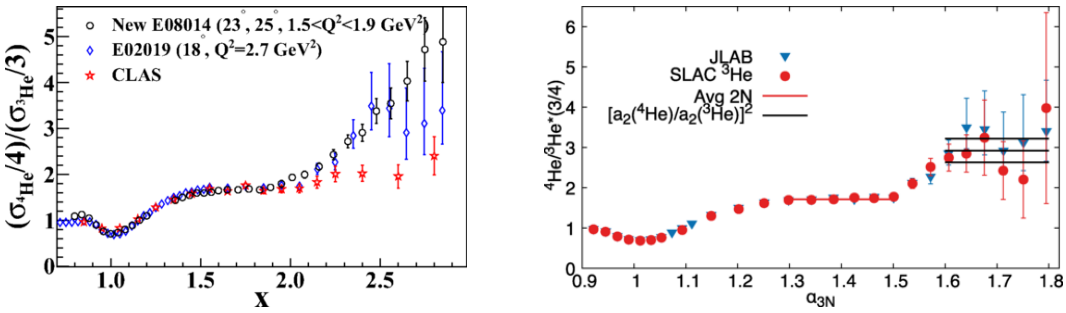


Figure 16: (a) JLab Hall A $(e, e')$ QE cross-section ratio of $^4$He to $^3$He showing no 3N-SRC plateau [64]. (b) Reanalysis of SLAC and Hall C data with a light cone variable indicating a possible 3N-SRC plateau [65]

evidence for modification of the partonic structure function of bound nucleons [31, 52, 53].

The observation of a correlation between the strength of the EMC effect and the SRC scaling coefficients in nuclei generated new interest in the EMC effect (see e.g. CERN Courier cover paper from May 2013; 'Deep in the nucleus: a puzzle revisited' [71]) and gave new insight into its possible origin. Several models have been proposed by us and others that attempt to explain the underlying dynamics that drive the EMC effect and its correlation with SRC pair abundances; see a recent review in Ref. [31].

In a data-mining analysis recently published in Nature [9], led by graduate student B. Schmookler and the spokespersons, a high-precision measurement of both the SRC scaling coefficients and the EMC effect was performed for $^{12}$C, $^{27}$Al, $^{56}$Fe and $^{208}$Pb (see Fig. 17). The new data were used to examine the finer aspects of the EMC-SRC correlation. Specifically, we examined whether the EMC data can indeed be explained by assuming the nuclear structure function can be factorized into a collection of un-modified mean-field nucleons and modified SRC pairs:

$$F_2^A = (Z - n_{\rm SRC}^A)F_2^p + (N - n_{\rm SRC}^A)F_2^n + n_{\rm SRC}^A \left(F_2^{p*} + F_2^{n*}\right), \quad (3)$$

where $n_{\rm SRC}^A$ is the number of $np$-SRC pairs, $F_2^N(x_B)$ are the free nucleon (proton and neutron) structure functions, and $F_2^{N*}(x_B)$ are the average modified nucleon structure functions in SRC pairs. $n_{\rm SRC}^A$ is taken from experiment (i.e. from $(e, e')$ scaling ratios at $x_B > 1.5$), and the modified

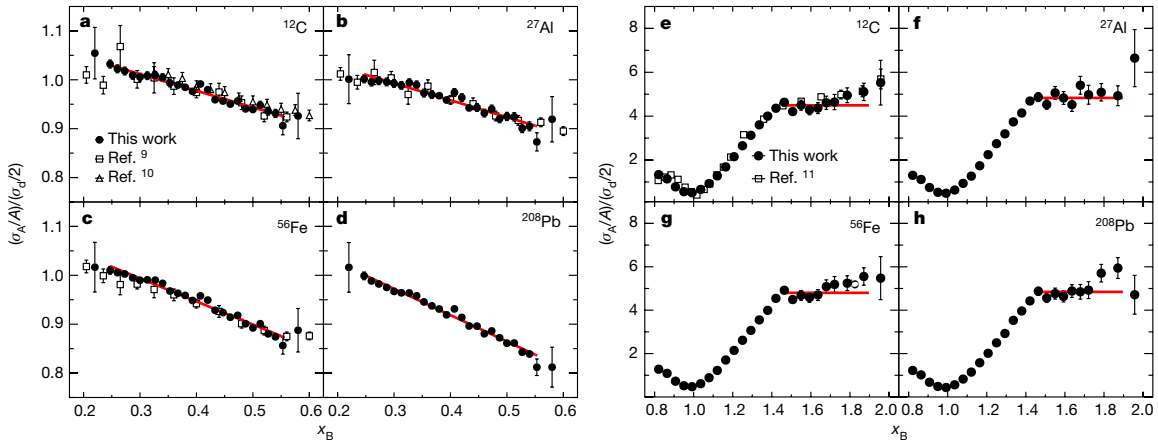


Figure 17: High-precision measurements of the EMC effect (left) and SRC scaling (right) led by the spokespersons [9].

structure function of SRC nucleons, $F_2^{N*}(x_B)$, is expected to be universal (i.e., independent of the surrounding nuclear environment).

Figure 18 shows the measured structure function ratios of nuclei relative to deuterium (left panel), and the extracted modification function of SRC pairs, using $\Delta F_2^N = F_2^{N*} - F_2^N$ (right panel). As can be seen, while the nuclear structure functions vary significantly between different nuclei, the extracted SRC pair modification function is universal for all nuclei.

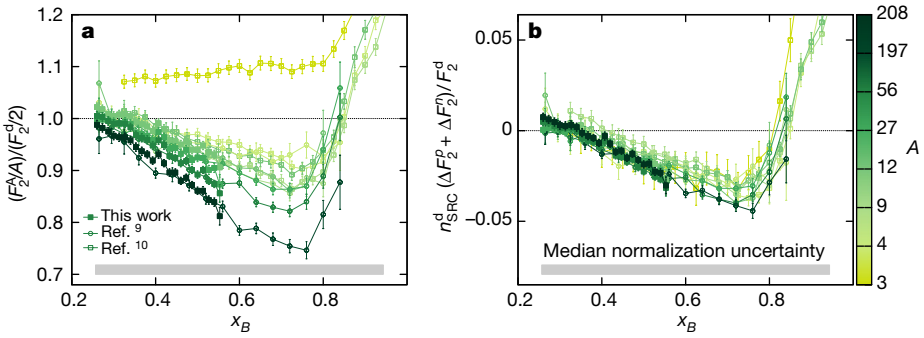


Figure 18: Left: measured structure function ratio for nuclei relative to deuterium (without model-dependent iso-scalar corrections). Right: the extracted universal modification function of nucleons in SRC pairs [9].

## 2.8 $J/\psi$ Photoproduction

Photoproduction of the $J/\psi$ meson from the proton was observed at both Cornell [72] ($E_\gamma = 11$ GeV) and SLAC [73] ($E_\gamma = 19$ GeV) soon after the discovery of the particle. Since the first observation of the phenomenon $J/\psi$ photoproduction have come to be understood as largely resulting from the exchange of gluons [74–76]. The 12-GeV upgrade to Jefferson Lab has enabled the first detailed differential measurements of $J/\psi$ photoproduction near the photoproduction threshold energy of $E_\gamma \approx 8.2$ GeV.

A 2019 study by GlueX [25] used real photon-proton data measured in Hall D to perform the first exclusive measurement of the $\gamma p \to J/\psi p$ cross section in the threshold region, spanning the photon

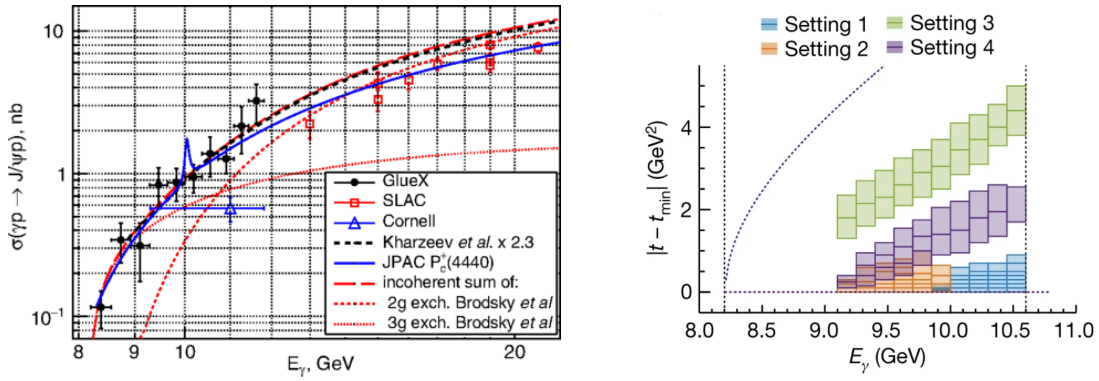


Figure 19: Measurements of $J/\psi$ photoproduction a Jefferson Lab. Left: The total cross section $\sigma(\gamma p \to J/\psi p)$ as a function of $E_\gamma$ from Ref. [25]. Right: Kinematic coverage of the measurement $\frac{d\sigma}{dt}(\gamma p \to J/\psi p)$ in bins of $E_\gamma$ and $t$ from Ref. [26].

energy range $8.2 < E_\gamma < 11.8$ GeV. This study measured both the total $J/\psi$ production cross section as a function of photon energy $E_\gamma$ (shown in Fig. 19) and the energy-integrated differential cross section as a function of 4-momentum transfer $t$.

As the first precision $J/\psi$ photoproduction data in the threshold region, this measurement provided substantial new insight into the gluonic structure of the proton not previously possible. The measurement has enabled insights into the gluonic/mechanical radius of the proton [77, 78], has been interpreted under the frameworks of gluon Generalized Parton Distributions (GPDs) [79] and holographic QCD [80], and has aided in understanding the proton mass by allowing extraction of the proton "trace anomaly" mass term [81].

A 2023 study [26] used real photon-proton data measured in Hall C to perform the first double-differential measurement of $J/\psi$ photoproduction. While this measurement was not exclusive, detecting only the $J/\psi \to e^+e^-$ decay, the high luminosity of a spectrometer-based measurement allowed detailed measurements of $\frac{d\sigma}{dt}(\gamma p \to J/\psi p)$ as a function of both $E_\gamma$ and $t$. The double-differential nature of this measurement allowed for detailed determination of gluonic gravitational form factors (GFFs) for the proton and higher-precision extraction of the proton trace anomaly mass. Theoretical analysis of this data was performed using both GPD [79] and holographic QCD [80] and was benchmarked against lattice QCD (LQCD) calculations for the proton [82]. The holographic QCD framework was found to agree particularly well with LQCD predictions, which provides further insight into the reaction mechanisms of $J/\psi$ photoproduction near threshold and enables more precise interpretation of future $J/\psi$ data.

# 3 Physics Goals

## 3.1 High-Statistics SRC Measurements

Existing photonuclear data enable initial measurements of SRC breakup to a similar level of precision to 6 GeV electron-scattering measurements. However, these data are insufficient to provide detailed tests of the reaction mechanisms needed to interpret the results. The reactions desired for measuring SRC properties are quasi-elastic-like (QE) meson photoproduction events, wherein the incident photon interacts solely with a single nucleon in an SRC pair, producing a meson and a baryon in the final state, as well as a high-momentum recoil nucleon which was a spectator to the reaction. This final-state may be produced through other reaction mechanisms which can complicate the interpretation of data. Coupling to Meson-Exchange Currents (MEC) or other multi-body reactions can result in a similar final state with multiple nucleons knocked out of the nucleus. Additionally, Final-State Interactions (FSI) in which the produced particles rescatter with one another or the residual nucleus can further impact the observed distributions. These effects differ substantially in photoproduction as compared with quasi-elastic electron-scattering, and have not been studied experimentally in these kinematics.

The high-statistics measurement proposed here is focused on a single nucleus and will enable detailed tests of these reaction mechanisms. A key goal of this experiment is to maximize the reach of the data over a large range of momentum transfer $|t|$. At large values of $|t|$, multi-body reactions such as MEC are suppressed relative to QE reactions, allowing for cleaner extraction of SRC properties. As photoproduction cross sections fall exponentially with $|t|$ for forward production, an increase in statistics by an order of magnitude allows for much higher values of $|t|$ to be observed in data. This allows for more stringent cuts to be placed on $|t|$ in order to isolate clean SRC breakup data. Additionally, the reaction mechanisms may be studied themselves by examining the dependence of our observables on $|t|$, what we term the "resolution-dependence" of the reaction. We expect some variation in the measured quantities at low $|t|$, as non-QE reactions are present and contribute differently from QE interactions, but at larger $|t|$ this dependence should no longer be present. This resolution-dependence is being studied in electron-scattering by varying the momentum-transfer $Q^2$, but a similar test has not yet been possible in photoproduction.

This measurement will also allow us to better determine the impact of FSI on the SRC breakup signal. FSI is strongly dependent on the angular orientation of the initial nucleon momentum, requiring control over the final-state kinematics to minimize. The high-statistics data obtained in this measurement will enable tests of the angular dependence of the data, enabling us to disentangle the effects of FSI on SRC photoproduction observables.

## 3.2 Three-Nucleon SRCs

In addition to providing detailed measurements of Two-Nucleon (2N) SRCs, this data would enable us to search for exclusive signals of Three-Nucleon (3N) SRC breakup. 3N-SRCs remain poorly-known [12], with much remaining to be learned regarding their abundance, formation, and structure. Of the possible configurations of 3N-SRCs, it is not known which dominate in nuclei, and how momentum is distributed between the three nucleons. Detailed study of 3N-SRC structure can give understanding both to the formation mechanisms involved and to the details of irreducible three-nucleon forces at short distance, which should strongly influence the momentum distributions within the triple. To perform such studies, exclusive measurements of 3N-SRC breakup over a wide range of kinematics are necessary.

Recent data from Hall B could enable exclusive measurements of 3N-SRC breakup [59]. However, FSI and background limit the kinematic space available to electron-scattering. In particular, electron-scattering measurements of SRC are largely limited to $x_B > 1.2$ to suppress FSI and inelastic backgrounds. This requirement allows access only to a fraction of possible 3N-SRC states due to the large binding energy involved and the necessary energy transfer to liberate the system.

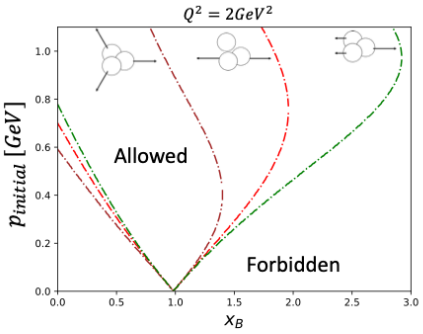


Figure 20: The allowed phase space for quasi-elastic scattering off an SRC is in the region above the curve while the forbidden phase space is the region below the curve. The red curve represents the 2 nucleon SRC. The brown curve represents a 3 nucleon SRC where all nucleons carry equal momenta (star configuration). The green curve represents a 3 nucleon SRC where the struck nucleon carries twice the momentum of its recoiling partners (rocket configuration).

Fig. 20 shows the allowed kinematic phase space for quasi-elastic electron scattering from $^3$He at $Q^2 = 2$ GeV$^2$ for different configurations of the 3 nucleons. In the 2N-SRC case (red), also included in the figure, the kinematic range extends nearly to $x_B = 2$. Values of $x_B$ around and below 1 can have large backgrounds caused by inelastic scattering and final-state interactions. For this reaction, electron-scattering studies of SRC breakup are typically restricted to $x_B > 1.2$.

In the case of 3N-SRCs, there are several possible momentum configurations of the triplet. In the "rocket" configuration (green), the kinematic range extends nearly to $x_B = 3$, and standard electron-scattering experiments with $x_B > 1.2$ are therefore capable of accessing probing these triplets. However, the "star" configuration (brown) is much more limited in kinematic phase space. A maximum $x_B$ of 1.3 is possible in this configuration, and that only for a narrow range of initial nucleon momentum. Electron-scattering experiments are therefore incapable of measuring the star configuration without extending to low $x_B$ and contending with the contamination from inelastic backgrounds.

Quasi-elastic meson photoproduction provides not only an independent probe of SRCs from electron-scattering, but also access to different kinematics. Photoproduction cross sections favor parallel kinematics rather than anti-parallel, which differs from the requirements of high-$x_B$ electron-scattering. The cross sections for meson photoproduction are large momentum-transfer $|t|$ are described by "constituent counting rules" [83], which predict that the differential cross section falls with the center-of-mass energy by $d\sigma/dt \sim s^{-7} \times f(\theta_{cm})$. This cross section heavily favors nucleon motion in the direction of the photon, whereas the requirement of large-$x_B$ favors nucleon motion opposite the virtual photon. This difference in kinematics means that photon-scattering probes the equivalent kinematic region of $x_B < 1$, while being less susceptible to inelastic backgrounds present in electron-scattering. The combination of high-statistics data using electron-scattering and photon-scattering will enable measurement of exclusive 3N-SRC breakup over the full spectrum of possible configurations, which is necessary to fully characterize their properties.

An additional benefit of photoproduction in this case is the ability to measure initial-state neutrons via the production of charged mesons. This is particularly valuable because *n-p-p* triplets are expected to be favored over *p-p-p* due to spin and isospin effects. While measuring this triplet with electron-scattering requires overcoming the technical challenge of neutron detection, photon-scattering can instead use charge-exchange channels such as $(\gamma, \pi^- ppp)$ and $(\gamma, \rho^- ppp)$, allowing greater ease in probing this type of 3N-SRC.

### 3.3 Near- and Sub-Threshold $J/\psi$ from the Nucleus

Photoproduction of $J/\psi$ from nuclear targets provides the opportunity to perform probes of the gluonic structure of the nucleus, similar to recent studies on the proton [25, 26]. Incoherent $J/\psi$ photoproduction from nuclei is sensitive to the fluctuations of gluons within the nucleus [84], as well as the gluonic structure of the bound nucleon. The study of near-threshold $J/\psi$ photoproduction from nuclei would allow a first search for a gluonic EMC effect in the valence region of $x \sim 0.5$.

Of similar interest is the possibility of measuring sub-threshold photoproduction of $J/\psi$ [85]. In nuclei, the Fermi motion of nucleons enables production of $J/\psi$ at lower photon energies than the production threshold of $E_\gamma \approx 8.2$ GeV from the proton. Such production is predicted to be directly sensitive to the details of nuclear structure. At sub-threshold energies, the production of $J/\psi$ has a higher contribution from Short-Range Correlations, enabling a probe of the gluon structure of correlated nucleons. Sub-threshold production is also sensitive to a number of phenomena which could enhance its production, such as hidden-color or non-nucleonic states [76, 86] or interaction of the $J/\psi$ with the nuclear medium [87]. A detailed scan of nuclear $J/\psi$ photoproduction over the photon energy threshold is at this point only possible at JLab following the 12-GeV upgrade, and this would provide critical insights into the gluon structure of the nucleus.

A high-statistics measurement of $(\gamma, J/\psi\ p)$ photoproduction from $^4$He would enable a scan of the incoherent nuclear photoproduction cross section as a function of photon energy. The cross section can be measured with photon energies ranging from 7.5 GeV to the endpoint energy of 12 GeV. Optimal placement of the coherent photopeak can enable measurement of the cross section even below threshold, where the cross section is expected to be small. Measurements at

Detecting the proton in such events improves the mass resolution of the $J/\psi$, and additionally enables reconstruction of the initial-state momentum of the proton involved in quasi-free production. This semi-inclusive measurement will enable detailed study of the reaction mechanisms for sub-threshold production by examining the correlation between the initial nuclear motion and the photon energy of the reaction.

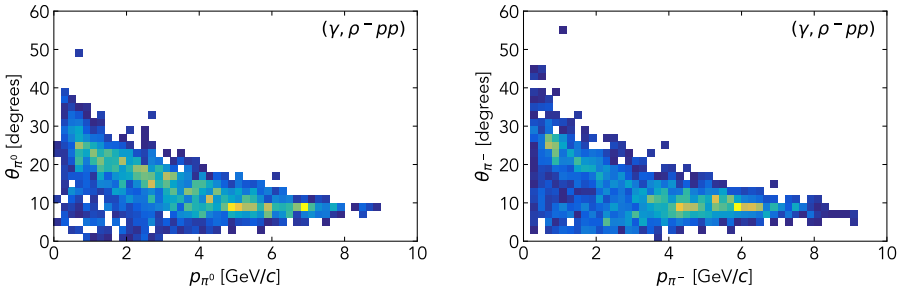


Figure 21: Kinematic distribution of the pions in measured data for $^4$He$(\gamma, \rho^- pp)$ with $|t| > 1.5$ GeV$^2$. Left: Kinematic distributions for the $\pi^0 \to \gamma\gamma$ decay, detected by the measurement of photon showers in the Forward and Barrel Calorimeter. Right: Kinematic distributions for the $\pi^-$ meson, detected by the measurement of charged tracks in the Forward and Central Drift Chambers.

# 4 Proposed Measurement

## 4.1 Final-State Kinematics and Particle Detection

### 4.1.1 SRC

There is a number of possible photoproduction channels that can be used to study hard SRC breakup. Of these we can select channels which maximize our ability to measure the reaction as desired; This typically means selecting channels with a high cross section, in order to maximize signal yields, and a distinctive final state, in order to reject backgrounds. Comparing multiple channels helps to better separate properties of the initial nuclear state from the reaction kinematics and nuclear many-body effects. Comparison of multiple final-state also helps to study detector systematics, which may differently impact the measurement of various meson decays (e.g. $\eta \to \gamma\gamma$ vs. $\eta \to \pi^+\pi^-\pi^0$).

As there are a large number of possible photoproduction channels to consider, we select here the representative channel of $\rho^-$ photoproduction from a neutron in a $n$-$p$ pair to simplify the picture and examine particle kinematics and detection. The final-state measured in the exclusive SRC breakup channel is $\rho^- pp \to (\pi^0\pi^-)pp \to ((\gamma\gamma)\pi^-)pp$. For the case of the $\pi^0 \to \gamma\gamma$ decay, the detection requires the measurement of the decay photons, which are observed by measuring "neutral" showers (with no corresponding charged track) in the Forward and Barrel calorimeters, which cover the angular ranges of $\theta_\gamma < 11°$ and $11° < \theta_\gamma < 126°$ respectively. Fig. 21(left) shows the kinematic distributions for the measured $\pi^0$ in existing $^4$He$(\gamma, \rho^- pp)$ data. We see no substantial effect of acceptance from the detectors; while events are focused at forward production angles this is largely an effect of the cross section falling rapidly with $t$.

The other final-state particles in this reaction are charged and can therefore be measured using the resulting charged tracks in the Forward and Central Drift Chambers. Fig. 21(right) shows the kinematic distributions for the charged $\pi^-$ meson in existing data. We note that this kinematic distribution is very similar to that for the $\pi^0$, which demonstrates that detector acceptance effects which would differentiate them are not present. In Fig. 22 we show the kinematic distributions for the final-state protons in $^4$He$(\gamma, \rho^- pp)$ data, including both the high-momentum "leading" proton from the hard reaction (left) and the lower-momentum "recoil" proton which was a spectator within the SRC pair. While cuts have been placed on these to ensure clear separation between the two protons in the event and remove ambiguity in the interpretation, we note no acceptance effects other than the detectors inability to resolve tracks with momentum below 0.4 GeV/$c$. We note that for the higher-momentum charged particles, the $\pi^-$ and the leading proton, the GlueX detector provides limited ability to perform reliable particle-identification. For lower-momentum charged particles

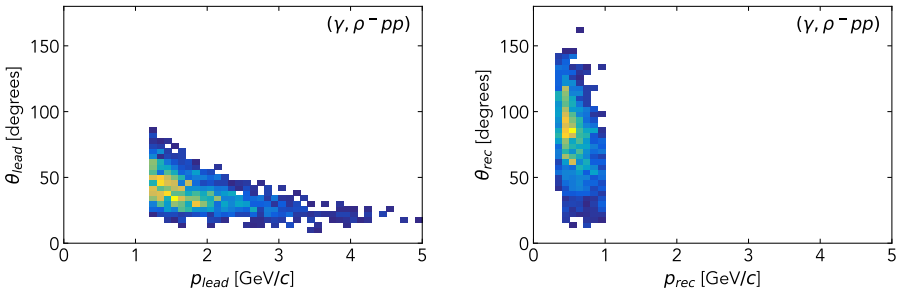


Figure 22: Kinematic distribution of the protons in measured data for $^4$He$(\gamma, \rho^- pp)$ with $|t| > 1.5$ GeV$^2$. Left: Kinematic distributions for the high-momentum "leading" proton. Right: Kinematic distributions for the lower-momentum "recoil" proton.

($p \lesssim 2.5$ GeV/$c$) in the forward direction ($\theta < 13°$), the scintillating Time-of-Flight detector may be used to perform measurements of $\beta$ and perform particle separation, but this covers only a fraction of the phase-space of these reactions. For the even lower-momentum recoil proton, particle identification may be reliably performed by examining measurements of $dE/dx$ in the straw-tube Central Drift Chamber, which allows particle separation to $p \sim 1$ GeV/$c$.

Rejection of backgrounds resulting from particle-misidentification has nonetheless been possible by leveraging understanding of the kinematics of the reaction for both the signal channel and the background. In the case of $^4$He$(\gamma, \rho^- pp)$, the largest background has been identified as diffractive multi-pion production $\gamma^4$He$\rightarrow \pi^0\pi^-\pi^+p$, with the misidentification of the $\pi^+$ as a high-momentum proton. Fig. 23 (left) shows the selection cut that has been used to achieve separation between SRC breakup events and this background channel. This takes advantage of the fact that diffractive multi-pion production like this is predominantly produced at very forward angles, whereas the knockout protons from quasi-elastic photoproduction are produced over a wide range of angles. This observation, along with understanding of the momentum balance of the two nucleons within an SRC pair, allows for the placement of a cut which allows clean isolation of SRC breakup data from this background. We also examine the invariant mass spectrum of the $\rho^- \rightarrow \pi^0\pi^-$ decay, shown in Fig. 23 after application of background cuts. We note that the level of background is very small compared to the $\rho^- \rightarrow \pi^0\pi^-$ decay peak at 775 MeV. The rejection of background resulting from particle-misidentification must be considered on a case-by-case basis for the different photoproduction channels. For this reason it is ideal to select channels with a similar invariant mass spectrum to examine. This test allows a means of quantifying the level of background present relative to signal, and helps in optimizing cuts to remove these backgrounds.

In standard GlueX running "kinematic fitting" is used to improve resolution on measured particle momentum. This method uses known constraints on the reaction in order to improve the reconstruction of poorly-measured kinematic variables. In the case of a proton target, often a fully exclusive final-state is measured. This enables the greatest power for kinematic fitting by requiring conservation of 4-momentum between the initial- and final-state. In the case of nuclear targets (other than deuterium), most hard reactions result in a residual nuclear state which is not measured. This reduces the utility of kinematic fitting, at the conservation of 4-momentum is by far the most strict constraint that can be applied. Other constraints on the reaction, such as a common reaction vertex between the particles and the invariant mass of an intermediate decay such as $\pi^0 \rightarrow \gamma\gamma$, can be applied and provide a modest improvement in the resolution of final-state particle momentum. However, the smearing of high-momentum particles in the GlueX detector still results in difficulties when attempting to reconstruct initial-state nuclear momentum. When we define the "missing"

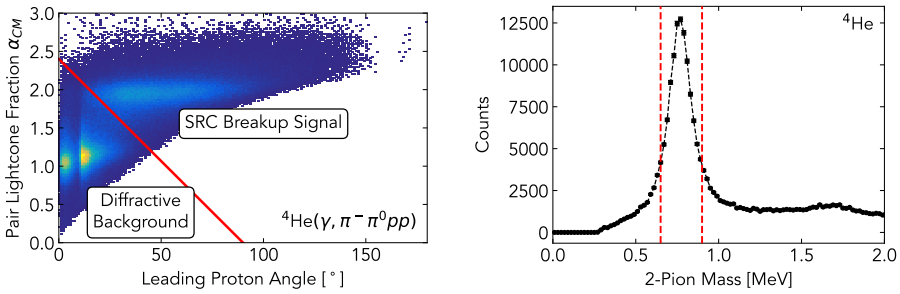


Figure 23: Left: The cut used to remove 3-pion diffractive background from $^4\mathrm{He}(\gamma, \rho^- pp)$ in data. To the bottom-left of the plot is the forward-peaked $\gamma^4\mathrm{He} \rightarrow \pi^0\pi^-\pi^+p$ background with the misidentification of the $\pi^+$ as a proton. To the top-right is the signal for SRC breakup. The red line denotes the cut used to separate the two. Right: The invariant mass spectrum for the decay $\rho^- \rightarrow \pi^0\pi^-$ in data. The decay peak can be clearly seen at 775 MeV.

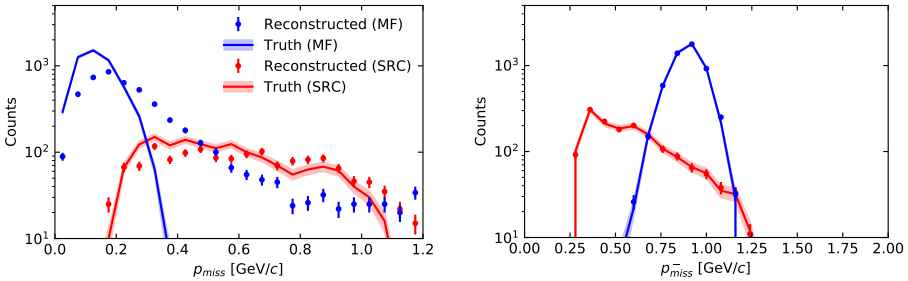


Figure 24: The effects of detector smearing on the inferred missing momentum in simulation are shown. Left: The effect of smearing on the magnitude of the reconstructed missing momentum. It can be seen that this smearing causes substantial bin migration, and particularly results in a large number of mean-field events reconstructed with large missing momentum. Right: The effect of smearing on the "minus" component of the missing momentum. Resolution effect can be seen to cause very little smearing or bin migration in this variable.

momentum for the initial-state neutron in $\rho^-$ photoproduction

$$p_{miss} = p_{\pi^0} + p_{\pi^-} + p_{lead} - p_{\gamma}\,, \tag{4}$$

we observe that the missing momentum, which is on the order of several hundred MeV, is obtained by subtracting the momentum of several GeV-scale particles. This results in substantial smearing on this variable, washing out any sensitivity to initial-state nuclear properties [88]; see Fig. 24(left).

This effect can be substantially mitigated by the use of "light-front" variables, which decompose the 4-momentum into the two "transverse" components of momentum perpendicular to the beamline

$$\vec{p}_{\perp} \equiv (p_x, p_y) \tag{5}$$

and into the linear combinations of the particle energy $E$ and the longitudinal momentum $p_z$

$$p^{\pm} \equiv E \pm p_z\,, \tag{6}$$

henceforth labelled the "plus" and "minus" components of momentum. These variables have previously been used in analysis of SRC breakup data [18] and can be used to address effects of momentum

smearing; while the "plus" component of missing momentum is subject to substantial smearing, the "minus" component is reconstructed extremely well, as seen in the simulations shown in Fig. 24. This can be understood as a cancellation in the definition of the variable, which leaves it relatively insensitive to smearing in $p_z$:

$$\frac{\partial p^-}{\partial p_z} = \frac{p_z}{E} - 1 = \mathcal{O}\left(p_\perp^2/p_z^2\right) \tag{7}$$

This effect, combined with the relatively small smearing for the transverse components of momentum in GlueX (a consequence of the solenoid magnet), provides us a combination of momentum variables that may be reliably used to describe the initial nuclear state.

While the details of measuring exclusive 3N-SRC breakup have not yet been established, it is likely that the same challenges will be present when using the GlueX spectrometer, and must be addressed in the same manner. Simulations of the signal process will be necessary to understand the kinematics of the reaction and to identify the kinematics of the measurement. The large number of potential signal channels will provide the opportunity to determine which final-state allow the greatest ability to isolate signal from background.

#### 4.1.2 $J/\psi$

The quasi-elastic channel $(\gamma, J/\psi p)$ was simulated using a factorized cross section model in the Plane-Wave Impulse Approximation (PWIA):

$$\frac{d\sigma(\gamma A \to J/\psi p X)}{dt d^3p_{miss} dE_{miss}} = K \cdot \frac{d\sigma}{dt}(\gamma p \to J/\psi p) \cdot S(p_{miss}, E_{miss}) \tag{8}$$

where $K$ is a kinematic flux factor, the differential cross section $d\sigma/dt$ for the exclusive process $(\gamma p \to J/\psi p)$ was taken from a fit to GlueX data [25], and the spectral function $S(p_{miss}, E_{miss})$ for Helium was taken from Ref. [89] for the mean-field component and the Generalized Contact Formalism [8, 39, 46] for the SRC component. The generated PWIA events were simulated using the GEANT description of the GlueX detector [90], and were reconstructed using standard GlueX reconstruction software in the same manner as measured data.

The kinematical distributions of the final-state particles in $(\gamma, J/\psi p)$ events are shown in Fig. 25 for production from mean-field proton and in Fig. 26 for SRC protons. For mean-field production, the leptons (electrons and positrons) have a wide kinematic distribution but a strong correlation between the momentum and angle of the particles; these kinematics are strongly controlled by kinematics of the decay $J/\psi \to e^+e^-$. The leptons as a result impact in both the Barrel Calorimeter (BCAL) and the Forward Calorimeter (FCAL). Particle identification for electrons and positrons is primarily possible in the GlueX detector by comparing the energy deposition into the calorimeters with the measured momentum of the charged track; for electrons and positrons, these values should have a ratio of $E_{dep}/p_{track} \sim 1$. The protons are consistently produced at low momentum $p_{proton} \sim 1$ GeV/$c$ and at moderate angles. The protons therefore primarily impact the BCAL, and additionally frequently have low enough momentum to allow particle identification using $dE/dx$ and time-of-flight. The kinematics for production from SRC protons are largely similar, with the largest difference being a wider kinematic distribution for the outgoing proton as a result of larger nuclear momentum.

A major consideration in the GlueX detector is resolving the peak of the $J/\psi \to e^+e^-$ decay. Using only the measured momentum of the leptons in the final state results in a reconstructed invariant mass with relatively poor resolution. As the $J/\psi \to e^+e^-$ decay sits atop a fairly substantial background of both Bethe-Heitler $e^+e^-$ and photoproduced $\pi^+\pi^-$, which cannot be reliably rejected by particle identification, improving the resolution of the peak is critical for achieving an accurate measure of the $J/\psi$ yield.

In standard GlueX proton-target configuration, kinematic fitting enables very sharp resolution of the $J/\psi$ mass peak [25]. The full exclusivity of the process $\gamma p \to J/\psi p$ allows for the constraint of total 4-momentum conservation, allowing for improvement in the resolution of poorly reconstructed

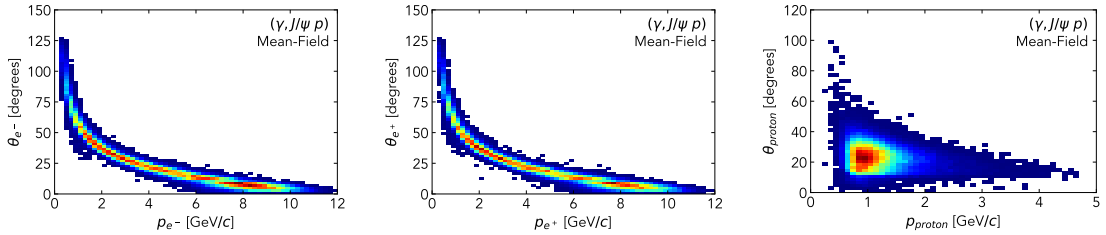


Figure 25: Simulated kinematic distributions for the final-state particles for $(\gamma, J/\psi p)$ production from mean-field protons. The electron (left) and positron (center) have a wide distribution of kinematics but a strong correlation between the momentum and the angle of the lepton. The proton (right) consistently is produced at moderate angles and low momentum.

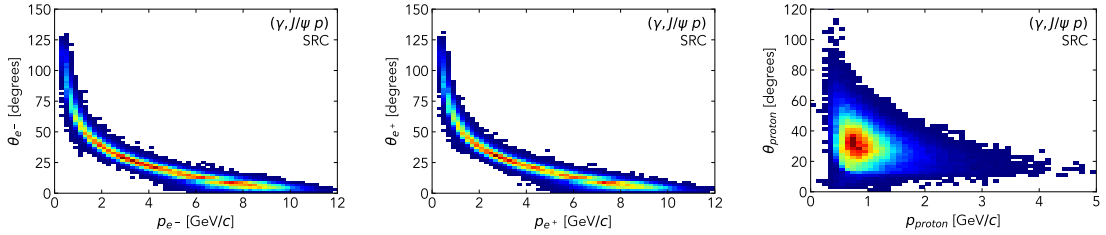


Figure 26: Simulated kinematic distributions for the final-state particles for $(\gamma, J/\psi p)$ production from SRC protons. Kinematics are similar to those events from mean-field protons, shown in Fig. 25

momentum components using those which are well-measured in the GlueX detector. In quasi-elastic photoproduction, total exclusivity may no longer be used to improve resolution to the same degree, but known kinematic constraints can still be used to improve resolution.

Using the previously described "light-front" components of momentum, we note that the "plus" component of momentum $p^+ \equiv E + p_z$ is poorly reconstructed for the high-momentum $J/\psi \to e^+e^-$ final-state. The low-momentum proton is more accurately reconstructed and may be used to constrain this component.

First, we note the "measured" value of the $J/\psi$ invariant mass:

$$m^2_{J/\psi,measured} = p^-_{J/\psi} \cdot p^+_{J/\psi} - p^2_{J/\psi,\perp} \tag{9}$$

where the 4-momentum $p_{J/\psi} \equiv p_{e^+} + p_{e^-}$ of the $J/\psi$ is calculated from those of the measured leptons. One assumption, which holds well for low nuclear momentum, is that of a standing proton with no initial momentum. In this case the invariant mass may be redefined by a simple substitution:

$$m^2_{J/\psi,stationary} = p^-_{J/\psi} \cdot (m_N + 2E_\gamma - p^+_{proton}) - p^2_{J/\psi,\perp} \tag{10}$$

Another assumption may be that of a standing SRC pair: the initial proton has substantial momentum which is balanced only by a single on-shell spectator nucleon. We may define in this case a "recoil" nucleon with momentum

$$p_{rec} = p_{2N} + p_{beam} - p_{J/\psi} - p_{proton} \tag{11}$$

and may use this to redefine the $J/\psi$ mass:

$$m^2_{J/\psi,QE} = p^-_{J/\psi} \cdot \left( 2m_N + 2E_\gamma - p^+_{proton} - \frac{m^2_N + p^2_{rec,\perp}}{p^-_{rec}} \right) - p^2_{J/\psi,\perp} \tag{12}$$

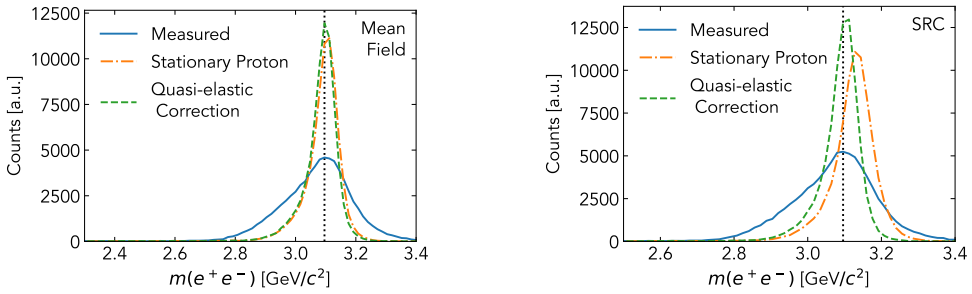


Figure 27: Simulated invariant dilepton mass for ($\gamma A \to J/\psi pX$), in the mean-field regime (left) and the SRC regime (right). The measured invariant mass (blue, solid) is poorly resolved and has a substantial tail at low invariant masses. The assumption of a standing proton (orange, dash-dot) improves the $J/\psi$ resolution for the mean-field case, but is shifted in the case of large nuclear motion for SRC protons. The two-body quasi-elastic correction to the mass (green, dashed) shows the largest improvement in the resolution for both cases.

In Fig. 27 we show these three methods of reconstructing the $J/\psi$ mass, both in the case of small nuclear motion (mean-field) and large motion (SRC). The measured mass value in each case is poorly reconstructed, with a large width and a substantial tail to lower masses. The assumption of the stationary proton works considerably better in the mean-field case, improving the resolution by a factor of $\sim 3$. This assumption is still an improvement in the SRC case, but deviates significantly from the true $J/\psi$ mass due to the large nuclear motion. The two-body quasi-elastic correction is shown to be a substantial improvement in both cases, matching the standing-proton assumption for the mean-field and improving upon it for SRC production. This correction can be seen to be generally effective for allowing efficient reconstruction of the decay $J/\psi \to e^+e^-$.

We have also examined existing $\gamma^4$He data taken in the GlueX detector during the SRC-CT experiment to verify that this observable allows for successful identification of a $J/\psi \to e^+e^-$ peak above backgrounds. Fig. 28 shows the measured dilepton invariant mass for selected $\gamma^4\text{He} \to J/\psi pX$ events, with the application of particle-identification and fiducial cuts, as well as cuts on the energy-balance of the reaction to remove accidental beam photons. The quasi-elastic correction of Eq. 12 has been applied to improve the $J/\psi$ mass resolution. It is clear that the application of this correction allows the resolution of the $J/\psi$ into a statistically significant peak above background. The total yield of $J/\psi$ events in this data is low, which is unsurprising given the total integrated nucleus-luminosity of 16.7 pb$^{-1}$ and the lower beam energy during the run.

We also use simulation to estimate the efficiency of detecting $\gamma^4\text{He} \to J/\psi pX$ events. Stringent cuts must be placed on data to remove the large backgrounds contributing to an apparently-similar final-state, and it is necessary to quantify the impact of these selection criteria, along with detector efficiency, on the measured signal yield. Fig. 29 shows the simulated efficiency for generated $\gamma^4\text{He} \to J/\psi pX$ events as a function of the beam photon energy. This efficiency includes both the inherent detector effects and the impact of particle-identification, fiducial, and energy-balance cuts previously listed. We observe that the efficiency is roughly constant as a function of beam energy, and stays between $15 - 20\%$ over the simulated range. This efficiency is somewhat smaller than for the exclusive process $\gamma p \to J/\psi\ p$ in GlueX, but remains relatively high and sufficient for a differential measurement.

## 4.2 Coherent Photopeak Energy Optimization

The placement of the coherent peak of the diamond radiator has a significant impact upon the photon flux as a function of $E_\gamma$, and is therefore of greatest relevance when considering the measurement

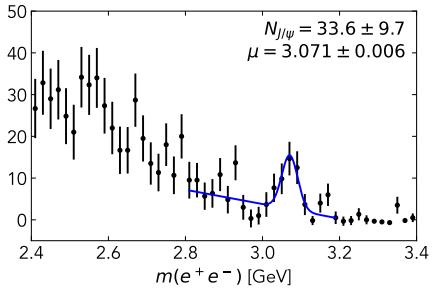


Figure 28: Measured dilepton invariant mass for $\sigma(\gamma^4\text{He} \to J/\psi pX)$ during the previous SRC-CT experiment in Hall D. The quasi-elastic correction of Eq. 12 is used here in reconstructing the mass. The $J/\psi$ mass peak can be seen at around 3.07 GeV, slightly shifted from the known value. In blue is a fit using a Gaussian signal and a linear background.

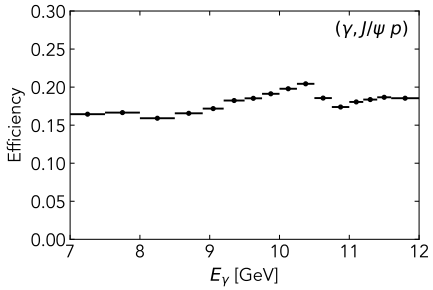


Figure 29: Total efficiency for measuring $\gamma^4\text{He} \to J/\psi pX$ events as a function of $E_\gamma$, calculated using simulation. The efficiency is simulated to be between $15 - 20\%$ and roughly constant with $E_\gamma$.

of the $J/\psi$ incoherent cross section. The placement of the coherent peak was selected in order to maximize our ability to measure the sub-threshold cross section for $J/\psi$ from $^4$He. A coherent peak at 8 GeV greatly enhances the tagged luminosity below the $J/\psi$ threshold, and results in an estimated $\sim 40$ measured $J/\psi$ events from beam photons with energies $E_\gamma < 8$ GeV.

A smaller coherent peak energy of 7.5 GeV was also considered, in order to improve the measurement in the deeper sub-threshold region of $E_\gamma < 7.5$ GeV. It was found that the total number of $J/\psi$ events with $E_\gamma < 8$ GeV was reduced to 20 in this case, with only a small relative enhancement to the $E_\gamma < 7.5$ GeV bin (which remains below 10 estimated events). This is primarily an effect of the fact that the Hall D Tagger Hodoscope for $E_\gamma \lesssim 7.8$ GeV is only a sampling tagger, and has only a 50% acceptance for the tagging of beam photons. As a result of this, and the very low predicted $J/\psi$ cross section for these photon energies, it is challenging to optimize for a reasonable measurement of the $J/\psi$ deeply-sub-threshold cross section with $E_\gamma < 7.5$ GeV.

For completeness we also considered a coherent peak energy at an energy of 9 GeV. This increases the average beam photon energy and results in an increased total $J/\psi$ yield from $\sim 1300$ to $\sim 1700$. However, these increases are in photon energy ranges which are already predicted to have relatively high yields; the total number of $J/\psi$ events with $E_\gamma < 8$ GeV is again reduced to $\sim 20$.

In order to optimize the number of sub-threshold events, we found that a coherent peak energy of 8 GeV resulted in roughly twice as many events with $E_\gamma < 8$ GeV than the other two cases considered. We therefore select this as the optimal coherent peak for mapping out the process $\sigma(\gamma^4\text{He} \to J/\psi pX)$ as a function of beam photon energy.

It is worth noting that it could be possible to improve the tagging efficiency for lower photon energies by adding extra taggers to the "sampling" region of the Hall D Tagger Hodoscope. This could potentially improve the measurement of sub-threshold $J/\psi$ in the kinematic region $E_\gamma \lesssim 7.8$ GeV. However, the ability to implement this in Hall D requires further study, and this possibility was not factored into either the selection of the coherent peak energy or the estimated event rates.

For estimates in this proposal calculated using the projected flux, we assumed a tagged flux equivalent to the SRC-CT experiment [60], roughly $3.4 \times 10^7$ $\gamma$/s when summing over all energy bins. This results in an estimated integrated luminosity of $\sim 160$ pb$^{-1}$·nucleus ($E_\gamma > 6$ GeV), an increase over the SRC-CT $^4$He data by a factor of 10.

## 4.3 Expected Rates

### 4.3.1 Hard SRC Breakup Measurements

Current data measured on $^4$He enables us to estimate the event rates for the measured SRC yields. Using the event yields observed in current data, we scale by the expected 100 PAC days to determine the estimated number of events for each channel of interest at different values of momentum-transfer $t$. We show in Table 1 the projected rates for semi-inclusive $(\gamma, \rho^0 p)$ photoproduction from mean-field nucleons as well as for exclusive $(\gamma, \rho^0 pp)$ and $(\gamma, \rho^- pp)$, which probe 2N-SRC proton-proton $pp$ and neutron-proton $np$ pairs respectively. We also calculate the event rates for exclusive 3N-SRC breakup channels by estimating the relative abundance of 2N- and 3N-SRCs in $^4$He. We anticipate a high-statistics coverage of 2N-SRC breakup events, which extend well into the region of large $|t|$ and enable mapping out any $|t|$-dependence. For 3N-SRC breakup, we expect a modest yield of events with a sufficient momentum transfer of $|t| > 1.5$ GeV$^2$, though any harsher requirement on $|t|$ would substantially reduce event yields.

Table 1: Expected number of counts for various MF, 2N, and 3N knockout reactions for different values of momentum-transfer $t$.

| | MF | 2N-SRC | | 3N-SRC | |
|---|---|---|---|---|---|
| Reaction | $(\gamma, \rho^0 p)$ | $(\gamma, \rho^0 pp)$ | $(\gamma, \rho^- pp)$ | $(\gamma, \rho^0 ppp)$ | $(\gamma, \rho^- ppp)$ |
| # Events Projected $^4$He ($\lvert t\rvert > 1.5$ GeV$^2$) | 510k | 10k | 12k | 100 | 120 |
| # Events Projected $^4$He ($\lvert t\rvert > 2$ GeV$^2$) | 110k | 2.5k | 4.7k | 30 | 50 |
| # Events Projected $^4$He ($\lvert t\rvert > 3$ GeV$^2$) | 20k | 500 | 480 | 5 | 5 |

### 4.3.2 $J/\psi$ Photoproduction

The simulations of incoherent $J/\psi$ photoproduction described in Sec. 4.1.2 were used to perform yield estimates for 100 days of running. Fig. 30 (left) shows the estimated yield of semi-inclusive $(J/\psi p)$ events in bins of beam photon energy $E_\gamma$. We find that the estimated yields are sufficient to allow a differential measurement in $E_\gamma$, and to provide sufficiently fine binning to map out the cross section over the $J/\psi$ threshold while maintaining adequate statistics in each bin. Notably, we anticipate a yield of $\sim 40$ subthreshold $J/\psi$ photoproduction events in addition to roughly 1300 higher-energy events.

We also use these yields in bins of $E_\gamma$ to estimate the precision on the total incoherent cross section $\sigma(\gamma^4\text{He} \to J/\psi pX)$ as a function of $E_\gamma$, as shown in Fig. 30 (right). The fractional statistical uncertainties on the cross section are calculated as $1/\sqrt{N}$ for each bin. The uncertainties resulting from background statistics are estimated to be twice the systematic uncertainties. Other point-to-point systematic uncertainties are estimated to be 10%, and the overall normalization uncertainty is estimated to be 25%, in both cases similar to the previous GlueX study [25].

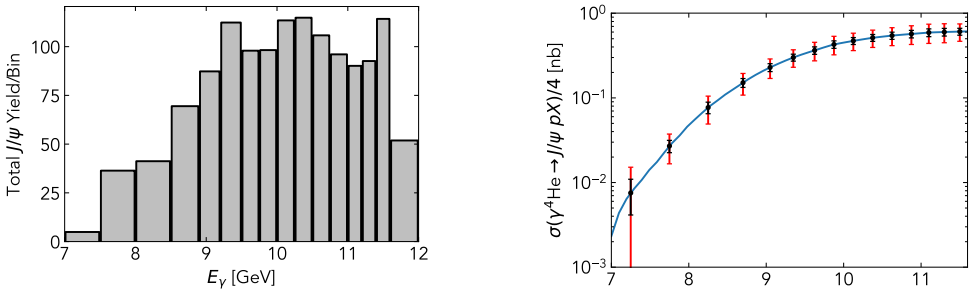


Figure 30: (Left): Projected yields for ($\gamma^4$He $\to J/\psi pX$) as a function of beam photon energy $E_\gamma$. Bin sizes were selected to provide a balance between the statistical uncertainties of the points. (Right): Projected measurement of $\sigma(\gamma^4\text{He} \to J/\psi pX)$ as a function of $E_\gamma$. In black are shown the estimated statistical uncertainties resulting from the measured $J/\psi \to e^+e^-$ yield. In red are the estimated total uncertainties, including the contributions from background and point-to-point systematic uncertainties. Not shown is an estimated 25% overall normalization uncertainty.

# 5 Relation to Other 12 GeV Experiments

The goal of this experiment is to perform the highest-statistics measurement of real photonuclear reactions at JLab energies. No equivalent dataset yet exists, but two complementary experiments should be noted.

The recent Hall D SRC-CT experiment E12-19-003 [60] measured 28 days of beam split between the nuclear targets $^2$H, $^4$He, and $^{12}$C. This experiment sought to perform first measurement of photonuclear probes of SRCs, as well as high-energy measurements of color-transparency in meson photoproduction reactions. This measurement lack the luminosity requested in this proposal, but has the benefit of examining multiple nuclei. This comparison between these nuclei allows for studying $A$-dependent phenomena in SRCs such as abundance and center-of-mass behavior. The interpretation of these data will be greatly aided by a the proposed high-statistics measurement of a single nucleus, which will aid in our understanding of the reaction mechanisms at play in these measurements. We note that these data also allow measuring the total $(\gamma, J/\psi\ p)$ cross section across these three nuclei when integrating over beam photon energy, but do not allow a differential measurement as proposed here.

The Hall B Run Group M measurement E12-17-006 [59] is another relevant measurement as the only other high-luminosity, large-acceptance measurement of SRC breakup in the 12-Gev era. This measurement has taken place and the data is being used to perform high-statistics studies of exclusive SRC breakup. The statistics of this measurement have allowed study of the reaction-mechanisms at play in electron-scattering measurements by examining the $Q^2$-dependence of observables. In addition, the large number of targets used in the experiment are allowing study of the $A$-dependence of exclusive SRC breakup reactions.

# 6 Summary

We propose a 100-day measurement using the real photon beam in Hall D, a $^4$He target, and the GlueX detector in its standard configuration, in order to study SRC breakup reactions, search for exclusive 3N-SRC breakup, and to measure nuclear $J/\psi$ photoproduction at and below the energy threshold. The high statistics of this measurement allows for precision study of the reaction mechanisms involved in photoproduction breakup of SRCs, complementing similar study of reaction mechanisms using SRC measurements in Hall B. The high luminosity also allows for a large number of $J/\psi$ events over a wide energy range, allowing for a detailed probe of high-$x$ gluons in the nucleus not possible at other facilities.

# References


[1] L. L. Frankfurt and M. I. Strikman, "Hard Nuclear Processes and Microscopic Nuclear Structure," *Phys. Rept.*, vol. 160, pp. 235–427, 1988.

[2] L. Frankfurt, M. Sargsian, and M. Strikman, "Recent observation of short range nucleon correlations in nuclei and their implications for the structure of nuclei and neutron stars," *Int. J. Mod. Phys. A*, vol. 23, pp. 2991–3055, 2008.

[3] C. Ciofi degli Atti, "In-medium short-range dynamics of nucleons: Recent theoretical and experimental advances," *Phys. Rept.*, vol. 590, pp. 1–85, 2015.

[4] A. Tang *et al.*, "*n-p* short range correlations from $(p, 2p + n)$ measurements," *Phys. Rev. Lett.*, vol. 90, p. 042301, 2003.

[5] I. Korover *et al.*, "Probing the Repulsive Core of the Nucleon-Nucleon Interaction via the $^4He(e, e'pN)$ Triple-Coincidence Reaction," *Phys. Rev. Lett.*, vol. 113, no. 2, p. 022501, 2014.

[6] R. Subedi *et al.*, "Probing Cold Dense Nuclear Matter," *Science*, vol. 320, pp. 1476–1478, 2008.

[7] M. Duer *et al.*, "Direct Observation of Proton-Neutron Short-Range Correlation Dominance in Heavy Nuclei," *Phys. Rev. Lett.*, vol. 122, no. 17, p. 172502, 2019.

[8] A. Schmidt *et al.*, "Probing the core of the strong nuclear interaction," *Nature*, vol. 578, no. 7796, pp. 540–544, 2020.

[9] B. Schmookler *et al.*, "Modified structure of protons and neutrons in correlated pairs," *Nature*, vol. 566, no. 7744, pp. 354–358, 2019.

[10] M. Duer *et al.*, "Probing high-momentum protons and neutrons in neutron-rich nuclei," *Nature*, vol. 560, no. 7720, pp. 617–621, 2018.

[11] O. Hen *et al.*, "Measurement of transparency ratios for protons from short-range correlated pairs," *Phys. Lett. B*, vol. 722, pp. 63–68, 2013.

[12] N. Fomin, D. Higinbotham, M. Sargsian, and P. Solvignon, "New Results on Short-Range Correlations in Nuclei," *Annual Review of Nuclear and Particle Science*, vol. 67, pp. 129–159, oct 2017.

[13] K. S. Egiyan *et al.*, "Measurement of 2- and 3-nucleon short range correlation probabilities in nuclei," *Phys. Rev. Lett.*, vol. 96, p. 082501, 2006.

[14] J. Arrington, N. Fomin, and A. Schmidt, "Progress in understanding short-range structure in nuclei: An experimental perspective," *Annual Review of Nuclear and Particle Science*, vol. 72, no. 1, pp. 307–337, 2022.

[15] R. Cruz-Torres *et al.*, "Comparing proton momentum distributions in $A = 2$ and 3 nuclei via $^2$H $^3$H and $^3$He $(e, e'p)$ measurements," *Phys. Lett. B*, vol. 797, p. 134890, 2019.

[16] S. Li, R. Cruz-Torres, N. Santiesteban, *et al.*, "Revealing the short-range structure of the mirror nuclei $^3$H and $^3$He," *Nature*, vol. 609, pp. 41–45, 2022.

[17] D. Nguyen *et al.*, "Novel observation of isospin structure of short-range correlations in calcium isotopes," *Phys. Rev. C*, vol. 102, p. 064004, Dec 2020.

[18] E. Piasetzky, M. Sargsian, L. Frankfurt, M. Strikman, and J. W. Watson, "Evidence for the strong dominance of proton-neutron correlations in nuclei," *Phys. Rev. Lett.*, vol. 97, p. 162504, 2006.

[19] M. Patsyuk *et al.*, "Unperturbed inverse kinematics nucleon knockout measurements with a 48 GeV/c carbon beam," *Nature Phys.*, vol. 17, p. 693, 2021.

[20] O. Hen *et al.*, "Momentum sharing in imbalanced Fermi systems," *Science*, vol. 346, pp. 614–617, 2014.

[21] R. Weiss, B. Bazak, and N. Barnea, "Generalized nuclear contacts and momentum distributions," *Phys. Rev.*, vol. C92, no. 5, p. 054311, 2015.

[22] R. Weiss, R. Cruz-Torres, N. Barnea, E. Piasetzky, and O. Hen, "The nuclear contacts and short range correlations in nuclei," *Phys. Lett.*, vol. B780, pp. 211–215, 2018.

[23] Hen, O. and others, "Exclusive Studies of Short Range Correlations in Nuclei using CLAS12 Proposal to Jefferson Lab PAC 46." Proposal PR12-17-007 to PAC46, 2018.

[24] O. Hen *et al.*, "Probing QCD in the nuclear medium with real photons and nuclear targets at GlueX." Proposal PR12-17-007 to PAC45, 2017.

[25] A. Ali *et al.*, "First Measurement of Near-Threshold $J/\psi$ Exclusive Photoproduction off the Proton," *Physical Review Letters*, vol. 123, Aug 2019.

[26] B. Duran *et al.*, "Determining the gluonic gravitational form factors of the proton," *Nature*, vol. 615, no. 7954, pp. 813–816, 2023.

[27] S. Afanasiev *et al.*, "Photoproduction of J/psi and of high mass e+e- in ultra-peripheral Au+Au collisions at s**(1/2) = 200-GeV," *Phys. Lett. B*, vol. 679, pp. 321–329, 2009.

[28] B. Abelev *et al.*, "Coherent $J/\psi$ photoproduction in ultra-peripheral Pb-Pb collisions at $\sqrt{s_{NN}} = 2.76$ TeV," *Physics Letters B*, vol. 718, pp. 1273–1283, jan 2013.

[29] E. Abbas *et al.*, "Charmonium and $e^+e^-$ pair photoproduction at mid-rapidity in ultra-peripheral Pb-Pb collisions at $\sqrt{s_{NN}} = 2.76$ TeV," *The European Physical Journal C*, vol. 73, nov 2013.

[30] S. Malace, D. Gaskell, D. W. Higinbotham, and I. Cloet, "The Challenge of the EMC Effect: existing data and future directions," *Int. J. Mod. Phys. E*, vol. 23, no. 08, p. 1430013, 2014.

[31] O. Hen, G. A. Miller, E. Piasetzky, and L. B. Weinstein, "Nucleon-Nucleon Correlations, Short-lived Excitations, and the Quarks Within," *Rev. Mod. Phys.*, vol. 89, no. 4, p. 045002, 2017.

[32] J. Arrington, D. W. Higinbotham, G. Rosner, and M. Sargsian, "Hard probes of short-range nucleon-nucleon correlations," *Prog. Part. Nucl. Phys.*, vol. 67, pp. 898–938, 2012.

[33] J. J. Kelly, "Nucleon knockout by intermediate-energy electrons," *Adv. Nucl. Phys.*, vol. 23, pp. 75–294, 1996. [,75(1996)].

[34] T. De Forest, "Off-Shell electron Nucleon Cross-Sections. The Impulse Approximation," *Nucl. Phys.*, vol. A392, pp. 232–248, 1983.

[35] C. Colle, W. Cosyn, and J. Ryckebusch, "Final-state interactions in two-nucleon knockout reactions," *Phys. Rev.*, vol. C93, no. 3, p. 034608, 2016.

[36] M. M. Sargsian, "Selected topics in high energy semiexclusive electronuclear reactions," *Int. J. Mod. Phys.*, vol. E10, pp. 405–458, 2001.

[37] S. N. More, S. K. Bogner, and R. J. Furnstahl, "Scale dependence of deuteron electrodisintegration," *Phys. Rev.*, vol. C96, no. 5, p. 054004, 2017.

[38] J. Carlson, S. Gandolfi, F. Pederiva, S. C. Pieper, R. Schiavilla, K. E. Schmidt, and R. B. Wiringa, "Quantum Monte Carlo methods for nuclear physics," *Rev. Mod. Phys.*, vol. 87, p. 1067, 2015.

[39] R. Weiss, I. Korover, E. Piasetzky, O. Hen, and N. Barnea, "Energy and momentum dependence of nuclear short-range correlations - Spectral function, exclusive scattering experiments and the contact formalism," *Phys. Lett.*, vol. B791, pp. 242–248, 2019.

[40] R. Cruz-Torres, A. Schmidt, G. A. Miller, L. B. Weinstein, N. Barnea, R. Weiss, E. Piasetzky, and O. Hen, "Short range correlations and the isospin dependence of nuclear correlation functions," *Phys. Lett.*, vol. B785, pp. 304–308, 2018.

[41] R. Weiss, A. Schmidt, G. A. Miller, and N. Barnea, "Short-range correlations and the charge density," *Phys. Lett.*, vol. B790, pp. 484–489, 2019.

[42] E. O. Cohen *et al.*, "Center of Mass Motion of Short-Range Correlated Nucleon Pairs studied via the $A(e, e'pp)$ Reaction," *Phys. Rev. Lett.*, vol. 121, no. 9, p. 092501, 2018.

[43] C. Ciofi degli Atti and S. Simula, "Realistic model of the nucleon spectral function in few and many nucleon systems," *Phys. Rev. C*, vol. 53, p. 1689, 1996.

[44] C. Colle, W. Cosyn, J. Ryckebusch, and M. Vanhalst, "Factorization of exclusive electron-induced two-nucleon knockout," *Phys. Rev. C*, vol. 89, no. 2, p. 024603, 2014.

[45] R. B. Wiringa, R. Schiavilla, S. C. Pieper, and J. Carlson, "Nucleon and nucleon-pair momentum distributions in $A \leq 12$ nuclei," *Phys. Rev. C*, vol. 89, no. 2, p. 024305, 2014.

[46] J. Pybus, I. Korover, R. Weiss, A. Schmidt, N. Barnea, D. Higinbotham, E. Piasetzky, M. Strikman, L. Weinstein, and O. Hen, "Generalized contact formalism analysis of the $^4$He$(e, e'pN)$ reaction," *Physics Letters B*, vol. 805, p. 135429, 2020.

[47] I. Korover *et al.*, "12C(e,e'pN) measurements of short range correlations in the tensor-to-scalar interaction transition region," *Phys. Lett. B*, vol. 820, p. 136523, 2021.

[48] R. B. Wiringa, V. G. J. Stoks, and R. Schiavilla, "An Accurate nucleon-nucleon potential with charge independence breaking," *Phys. Rev.*, vol. C51, pp. 38–51, 1995.

[49] A. Gezerlis, I. Tews, E. Epelbaum, S. Gandolfi, K. Hebeler, A. Nogga, and A. Schwenk, "Quantum Monte Carlo Calculations with Chiral Effective Field Theory Interactions," *Phys. Rev. Lett.*, vol. 111, no. 3, p. 032501, 2013.

[50] T. Neff and H. Feldmeier, "The Wigner function and short-range correlations in the deuteron," *arXiv:1610.04066*, 2016.

[51] J.-W. Chen, W. Detmold, J. E. Lynn, and A. Schwenk, "Short Range Correlations and the EMC Effect in Effective Field Theory," *Phys. Rev. Lett.*, vol. 119, no. 26, p. 262502, 2017.

[52] C. Ciofi degli Atti, L. L. Frankfurt, L. P. Kaptari, and M. I. Strikman, "On the dependence of the wave function of a bound nucleon on its momentum and the EMC effect," *Phys. Rev.*, vol. C76, p. 055206, 2007.

[53] S. A. Kulagin and R. Petti, "Structure functions for light nuclei," *Phys. Rev. C*, vol. 82, p. 054614, 2010.

[54] R. Schiavilla, R. B. Wiringa, S. C. Pieper, and J. Carlson, "Tensor Forces and the Ground-State Structure of Nuclei," *Phys. Rev. Lett.*, vol. 98, p. 132501, 2007.

[55] M. M. Sargsian, T. V. Abrahamyan, M. I. Strikman, and L. L. Frankfurt, "Exclusive electrodisintegration of $^3$He at high $Q^2$. II. Decay function formalism," *Phys. Rev. C*, vol. 71, p. 044615, 2005.

[56] M. Alvioli, C. Ciofi degli Atti, and H. Morita, "Proton-neutron and proton-proton correlations in medium-weight nuclei and the role of the tensor force," *Phys. Rev. Lett.*, vol. 100, p. 162503, 2008.

[57] C. Colle, O. Hen, W. Cosyn, I. Korover, E. Piasetzky, J. Ryckebusch, and L. B. Weinstein, "Extracting the mass dependence and quantum numbers of short-range correlated pairs from $A(e, e'p)$ and $A(e, e'pp)$ scattering," *Phys. Rev.*, vol. C92, no. 2, p. 024604, 2015.

[58] M. Duer *et al.*, "Measurement of Nuclear Transparency Ratios for Protons and Neutrons," *Phys. Lett. B*, vol. 797, p. 134792, 2019.

[59] Hen, O. and others, "Jefferson Lab 12 GeV experiment E12-17-006A." https://www.jlab.org/exp_prog/proposals/18/PR12-18-003.pdf.

[60] O. Hen *et al.*, "Studying short-range correlations with real photon beams at gluex," 2020.

[61] N. Wright, A. Papadopoulou, J. R. Pybus, S. Gardiner, M. Roda, F. Hauenstein, A. Ashkenazi, L. B. Weinstein, A. Schmidt, and O. Hen, "Transport Estimations of Final State Interaction Effects on Short-range Correlation Studies Using the $(e, e'p)$ and $(e, e'pp)$ Reactions," 2021.

[62] M. M. Sargsian, D. B. Day, L. L. Frankfurt, and M. I. Strikman, "Searching for three-nucleon short-range correlations," *Phys. Rev. C*, vol. 100, no. 4, p. 044320, 2019.

[63] N. Fomin *et al.*, "New measurements of high-momentum nucleons and short-range structures in nuclei," *Phys. Rev. Lett.*, vol. 108, p. 092502, 2012.

[64] Z. Ye *et al.*, "Search for three-nucleon short-range correlations in light nuclei," *Phys. Rev. C*, vol. 97, p. 065204, Jun 2018.

[65] D. B. Day, L. L. Frankfurt, M. M. Sargsian, and M. I. Strikman, "Toward observation of three-nucleon short-range correlations in high-$Q^2 A(e, e^{'})X$ reactions," *Phys. Rev. C*, vol. 107, p. 014319, Jan 2023.

[66] L. L. Frankfurt, M. I. Strikman, D. B. Day, and M. Sargsian, "Evidence for short range correlations from high $Q^2$ $(e, e')$ reactions," *Phys. Rev.*, vol. C48, pp. 2451–2461, 1993.

[67] K. S. Egiyan *et al.*, "Observation of nuclear scaling in the $A(e, e')$ reaction at $x_B$ greater than 1," *Phys. Rev. C*, vol. 68, p. 014313, 2003.

[68] L. B. Weinstein, E. Piasetzky, D. W. Higinbotham, J. Gomez, O. Hen, and R. Shneor, "Short Range Correlations and the EMC Effect," *Phys. Rev. Lett.*, vol. 106, p. 052301, 2011.

[69] O. Hen, E. Piasetzky, and L. B. Weinstein, "New data strengthen the connection between Short Range Correlations and the EMC effect," *Phys. Rev.*, vol. C85, p. 047301, 2012.

[70] O. Hen, D. W. Higinbotham, G. A. Miller, E. Piasetzky, and L. B. Weinstein, "The EMC Effect and High Momentum Nucleons in Nuclei," *Int. J. Mod. Phys. E*, vol. 22, p. 1330017, 2013.

[71] D. W. Higinbotham, G. Miller, O. Hen, and K. Rith, "The EMC effect still puzzles after 30 years," *CERN Cour.*, p. 35, April 2013.

[72] B. Gittelman, K. M. Hanson, D. Larson, E. Loh, A. Silverman, and G. Theodosiou, "Photoproduction of the $\psi(3100)$ Meson at 11 GeV," *Phys. Rev. Lett.*, vol. 35, pp. 1616–1619, Dec 1975.

[73] U. Camerini, J. G. Learned, R. Prepost, C. M. Spencer, D. E. Wiser, W. Ash, R. L. Anderson, D. Ritson, D. Sherden, and C. K. Sinclair, "Photoproduction of the psi Particles," *Phys. Rev. Lett.*, vol. 35, p. 483, 1975.

[74] M. G. Ryskin, "Diffractive J / psi electroproduction in LLA QCD," *Z. Phys. C*, vol. 57, pp. 89–92, 1993.

[75] S. J. Brodsky, L. Frankfurt, J. F. Gunion, A. H. Mueller, and M. Strikman, "Diffractive leptoproduction of vector mesons in QCD," *Phys. Rev. D*, vol. 50, pp. 3134–3144, 1994.

[76] S. Brodsky, E. Chudakov, P. Hoyer, and J. Laget, "Photoproduction of charm near threshold," *Physics Letters B*, vol. 498, pp. 23–28, jan 2001.

[77] D. E. Kharzeev, "Mass radius of the proton," *Phys. Rev. D*, vol. 104, p. 054015, Sep 2021.

[78] R. Wang, W. Kou, Y.-P. Xie, and X. Chen, "Extraction of the proton mass radius from the vector meson photoproductions near thresholds," *Phys. Rev. D*, vol. 103, p. L091501, May 2021.

[79] Y. Guo, X. Ji, and Y. Liu, "Qcd analysis of near-threshold photon-proton production of heavy quarkonium," *Phys. Rev. D*, vol. 103, p. 096010, May 2021.

[80] K. A. Mamo and I. Zahed, "Nucleon mass radii and distribution: Holographic QCD, lattice QCD, and GlueX data," *Physical Review D*, vol. 103, may 2021.

[81] R. Wang, X. Chen, and J. Evslin, "The origin of proton mass from $J/\psi$ photo-production data," *The European Physical Journal C*, vol. 80, no. 6, p. 507, 2020.

[82] D. A. Pefkou, D. C. Hackett, and P. E. Shanahan, "Gluon gravitational structure of hadrons of different spin," *Physical Review D*, vol. 105, Mar 2022.

[83] S. J. Brodsky and G. R. Farrar, "Scaling Laws at Large Transverse Momentum," *Phys. Rev. Lett.*, vol. 31, pp. 1153–1156, Oct 1973.

[84] H. I. Miettinen and J. Pumplin, "Diffraction scattering and the parton structure of hadrons," *Phys. Rev. D*, vol. 18, pp. 1696–1708, Sep 1978.

[85] Y. Hatta, M. Strikman, J. Xu, and F. Yuan, "Sub-threshold J/$\psi$ and $\Upsilon$ production in $\gamma$A collisions," *Physics Letters B*, vol. 803, p. 135321, apr 2020.

[86] J.-M. Laget and R. Mendez-Galain, "Exclusive photo- and electroproduction of vector mesons at large momentum transfer," *Nuclear Physics A*, vol. 581, no. 3, pp. 397–428, 1995.

[87] S. J. Brodsky, I. Schmidt, and G. F. de Téramond, "Nuclear-bound quarkonium," *Phys. Rev. Lett.*, vol. 64, pp. 1011–1014, Feb 1990.

[88] Pybus, J. R. and Sharp, P. and Szumila-Vance, H., "Exploring short range correlations through $\gamma$n$\rightarrow \pi$- p in the GlueX detector." SRC/CT Collaboration analysis note, 2020.

[89] N. Rocco and A. Lovato. private communication.

[90] S. Adhikari *et al.*, "The GlueX beamline and detector," *Nuclear Instruments and Methods in Physics Research Section A: Accelerators, Spectrometers, Detectors and Associated Equipment*, vol. 987, p. 164807, jan 2021.